

Chapter 1

ANALYSIS AND CONTROL OF CHAIN MOBILITY IN PROTEIN HYDROGELS

1.1 Abstract

Coiled-coil domains can direct the assembly of protein block copolymers into physically crosslinked, viscoelastic hydrogels. Here we describe the use of fluorescence recovery after photobleaching (FRAP) to probe chain mobility in reversible hydrogels assembled from engineered proteins bearing terminal coiled-coil domains. We show that chain mobility can be related to the underlying dynamics of the coiled-coil domains by application of a 3-state “hopping” model of chain migration. We further show that genetic programming allows the effective mobility of network chains to be varied 500-fold through modest changes in protein sequence. Destabilization of the coiled-coil domains by site-directed mutagenesis increases the effective diffusivity of probe chains. Conversely, probe mobility is reduced by expanding the hydrophobic surface area of the coiled-coil domains through introduction of the bulky leucine surrogate homoisoleucine. Predictions from the 3-state model imply asymmetric sequential binding of the terminal domains. Brownian Dynamics simulations suggest that binding asymmetry is a general feature of reversible gels, arising from a loss in entropy as chains transition to a conformationally restricted bridged state.

1.2 Introduction

Protein engineering enables the design and synthesis of monodisperse polymers with functional domains drawn from nature or created *de novo* (1). Because protein polymers are

made by expression of artificial genes, they can be modified easily and systematically by editing of their DNA coding sequences. In this manner, proteins have been engineered with binding domains that drive them to self-assemble into physically crosslinked networks (2). The non-covalent nature of domain association in these networks permits the constituent proteins to exchange binding partners. Such processes are common in polymeric systems; for example, block copolymer micelles in solution exchange chains at rates that are highly dependent on the architectures of the individual blocks (3, 4), and telechelic polymers with hydrophobic endgroups form micellar networks that relax via chain disengagement from interconnected micelles (5). Exchange of polymeric strands also plays essential roles in biological processes, including repair of double-stranded DNA breaks by homologous recombination (6, 7).

Strand exchange dynamics are particularly important in governing the viscoelastic properties of hydrogels assembled from proteins that carry amphipathic α -helical domains (2, 8, 9). Amphipathic helices are ubiquitous in nature, and often function by driving protein aggregation through the formation of coiled-coil bundles (10-12). Hydrogels assembled from coiled-coil proteins are reversible: they can disassemble and reassemble rapidly in response to external stimuli such as temperature changes or mechanical shear (2). These hydrogels are also shear thinning, injectable and potentially useful for delivery of cellular or molecular therapeutics (13). Because strand exchange underlies the physical behavior of the network, tuning the strand exchange rate is essential for optimizing hydrogel performance.

Characterization of strand exchange in coiled-coil systems has largely been limited to

chromatographic analyses of equilibrium solutions (10, 14, 15), stopped-flow spectroscopy (16), and fluorescence dequenching experiments (9, 17). These techniques are most useful for analysis of dilute solutions, and cannot be applied directly to hydrogels. In contrast, fluorescence recovery after photobleaching (FRAP) is routinely used to assess macromolecular diffusion and binding in crowded environments such as the cellular milieu (18). For example, FRAP has been used to measure rates of binding of leucine-zipper transcription factors to chromatin in live cells (19). The method requires only minor perturbation of the system of interest through sparse labeling with fluorescent dyes, and is amenable to analysis by models that permit simultaneous determination of diffusion coefficients and binding constants (18, 20). Although FRAP has been used to probe chain mobility in polymer networks, strand exchange has either not been important in these systems (e.g. in covalently crosslinked networks) (21, 22), or has not been quantified (23-26). The technique is commonly used only to estimate effective chain diffusivity, and when interchain binding is present, it is typically assessed qualitatively.

This chapter describes the use of FRAP to characterize the interplay between strand exchange and chain mobility in associative protein hydrogels. The gels were formed from an engineered triblock protein (designated “PEP”) composed of two identical coiled-coil domains (“P”) at the N- and C-termini, flanking a water-soluble midblock (“E”) consisting of elastin-like polypeptide repeats (**Supplementary Table 1.1**). The P domain is derived from the N-terminal fragment of rat cartilage oligomeric matrix protein (COMP), and has been reported to form homopentameric coiled-coil bundles (8, 27). Association of the P domains drives the reversible assembly of PEP into optically transparent, physically

crosslinked networks. The viscoelastic behavior of PEP networks is analogous to that of other networks assembled by association of coiled-coil domains (13).

Here we use FRAP to determine diffusion coefficients and equilibrium binding constants of fluorescently labeled PEP chains in PEP hydrogels. We find that the mobility of PEP chains is significantly reduced by reversible network association. To gain insight into the mechanism of chain mobility, we elaborate a previously developed 2-state reaction-diffusion model for FRAP into a 3-state “hopping” model of chain migration (18, 20). We find experimentally and in coarse-grained Brownian Dynamics simulations of gel-forming telechelic polymers that binding of one of the P domains in PEP reduces binding of the second. Finally, we show that tracer chain mobility is highly sensitive to structural changes in the coiled-coil endblocks. Taken together, our results furnish a new framework for understanding and controlling chain mobility in reversible polymer networks.

1.3 Experimental

1.3.1 Hydrogel Preparation

All protein concentrations are reported in % (*w/v*). To prepare a 10% (*w/v*) gel, 100 μ L of phosphate buffer (100 mM, pH 7.2 – 7.4) was added directly to 10 mg of lyophilized PEP and the suspension was placed on ice to promote gelation. After 2 – 4 h on ice, hydration was usually complete as evidenced by the formation of an optically clear gel. In order to ensure network homogeneity, gels were typically heated above the gel-sol transition temperature (~75 °C for a 10% gel) by submerging them in boiling water for 30 – 60 s. Upon heating, even concentrated solutions of PEP (up to 30%) became viscous liquids. After heating,

samples were immediately placed back on ice to allow gels to reform. Alternatively, samples could be left on ice for 24 – 48 h without heating in order to obtain completely homogenous gels. Fluorescent hydrogels were prepared by adding low concentrations (typically mass ratios of 1:50 or 1:100 were used) of fluorescein-labeled probe chains to PEP networks.

1.3.2 Fluorescence Recovery after Photobleaching

Fluorescent hydrogels were placed between two glass slides separated by 120 μm spacers (Secure-Seal spacer, 9 mm \times 0.12 mm, Life Technologies). Photobleaching experiments were performed on a Zeiss LSM 5 Exciter inverted confocal microscope equipped with the following laser lines: 458, 488, 514, 543 and 633 nm. All lasers were typically applied during the bleaching period. Cylindrical bleach volumes of defined radius were created using the bleach applet in the Zen 2009 confocal microscopy software suite (Zeiss). A 20X objective was used for the large spot size experiments ($a = 12.5 - 25 \mu\text{m}$). 2000 iterations at a scan rate of 1.61 μs per pixel resulted in a well-resolved cylindrical bleach volume that penetrated the entire gel. Fluorescence recovery in the photobleached spot was monitored between 500 and 530 nm with a wide pinhole on a single z-slice in the center of the hydrogel. Images were typically collected at a rate of 1 s^{-1} and at a resolution of 256 \times 256 pixels. Fluorescence intensities within the photobleached spot were quantified using the Zen region-of-interest “mean ROI” applet. To account for non-specific photobleaching caused by image acquisition during spot recovery, all curves were normalized to the fluorescence intensity of a region far from the photobleached spot. Quantitative analysis of the fluorescence recovery curves was performed in MATLAB.

1.4 Results and Discussion

1.4.1 Reversible PEP hydrogels show fluorescence recovery after photobleaching

To probe chain mobility in PEP hydrogels, we generated a series of fluorophore-labeled probes that would associate with network junctions in a defined manner, without affecting the rheological behavior of the network. We first performed site-directed mutagenesis on PEP to introduce a single cysteine residue into the elastin-like midblock, resulting in PEcP (**Supplementary Table 1.1**). The absence of other cysteines in the protein enabled site-specific conjugation of fluorescein-5-maleimide (*f5m*) to the central thiol via Michael-type addition (**Figure 1.1A** and **Supplementary Figure 1.1**). The PEcP-*f5m* conjugate yielded homogeneous, fluorescent gels when added at low concentrations into PEP networks (typically PEcP to PEP ratios of 1:50-100 were used). Using oscillatory shear rheometry, we verified that the rheological behavior of PEP gels was minimally perturbed by this labeling strategy (**Supplementary Figure 1.2**).

Next we prepared fluorescent PEP hydrogels of defined thickness (~120 μm), and photobleached cylindrical volumes in each gel using a standard confocal microscope. In 10% weight-to-volume (*w/v*) gels, we observed steady recovery of fluorescence intensity within the photobleached spot (**Figure 1.1B**). Fluorescence recovery results from diffusion of unbleached fluorophore into the photobleached region, and confirms that PEcP chains are mobile within PEP networks. Consistent with our hypothesis that PEcP is associated with the network, we observed accelerated rates of fluorescence recovery in networks solubilized with 8 M urea, a common protein denaturant.

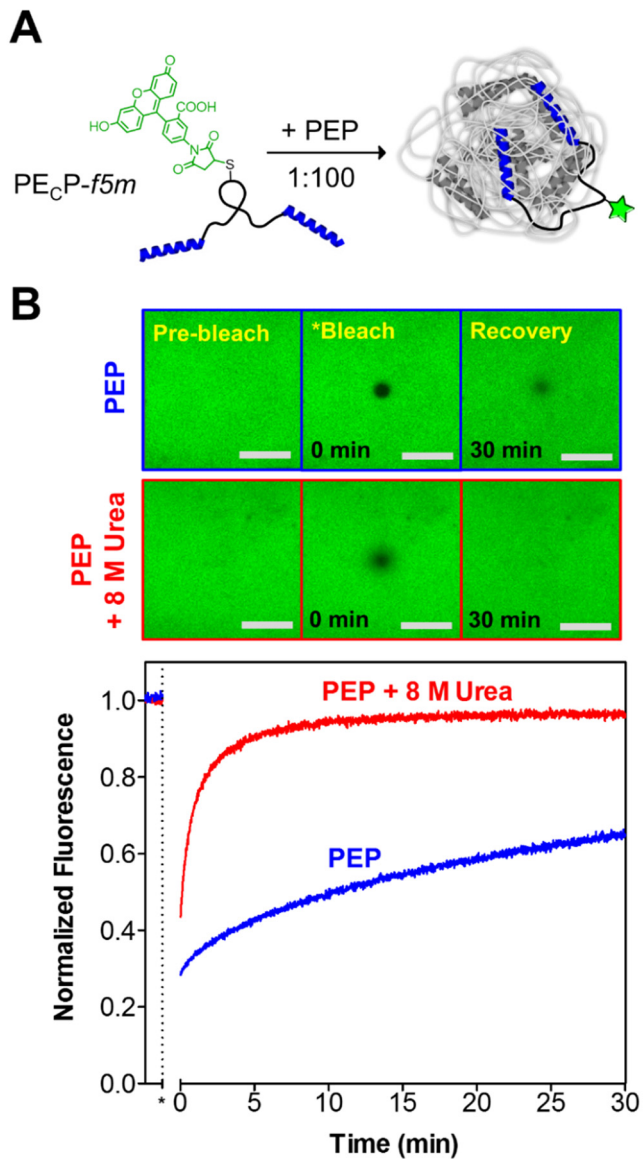


Figure 1.1. Fluorescence recovery after photobleaching in labeled PEP hydrogels. (A) Labeling of PEP hydrogels was achieved by addition of a fluorescent PEP analogue (PE_CP-*f5m*) at low concentrations. (B) FRAP in 10% *w/v* PEP hydrogels as monitored by confocal microscopy. A circular bleach spot with a radius of 12.5 μm recovers slowly over a period of 30 min (blue curve). The same network solubilized in 8 M urea shows accelerated fluorescence recovery (red curve). Scale bar 100 μm .

1.4.2 Quantitative analysis of chain mobility.

Gels were prepared at protein concentrations ranging from 2% to 10% *w/v* (gelation in PEP solutions occurs near 3%). As expected, the rate of fluorescence recovery after photobleaching decreased with increasing protein concentration (**Figure 1.2A**). To quantify chain mobility, we fit the experimental FRAP curves to a model that attributes fluorescence recovery to diffusion only (see **Supplementary Equations 23, 25 and 30**). Such an analysis is similar to standard FRAP analyses of diffusion in polymer networks (22, 23, 25, 26, 28), and results in a single parameter termed D_{eff} , the effective diffusion coefficient (18). In the case of PEP networks, fluorescence recovery represents diffusion slowed by binding; D_{eff} provides a measure of the mobility of polymer chains for which Brownian motion is constrained by reversible network association. The effective diffusion model yielded good fits to the fluorescence recovery curves (**Figure 1.2**), enabling us to estimate D_{eff} for each gel. D_{eff} decreases steeply with increasing protein concentration, dropping from 1.3×10^{-8} $\text{cm}^2 \text{ s}^{-1}$ in viscous 2% solutions to 2.3×10^{-10} $\text{cm}^2 \text{ s}^{-1}$ in 10% gels (**Figure 1.2B**).

We attribute the slower recovery at higher protein concentrations primarily to the increased concentration of binding sites, although changes in network topology such as loop suppression and chain entanglement may also suppress chain release from junctions (5, 8, 29). To explore whether the effective diffusivity is controlled by reversible endblock binding, we measured chain mobility as a function of the concentration of the protein denaturant urea. At a fixed protein concentration of 10%, the rate of fluorescence recovery increased abruptly with increasing concentration of urea (**Figure 1.2C**); addition of 2 M urea increases D_{eff} by 9-fold (**Figure 1.2D**). The abruptness of the change suggests that modest concentrations of

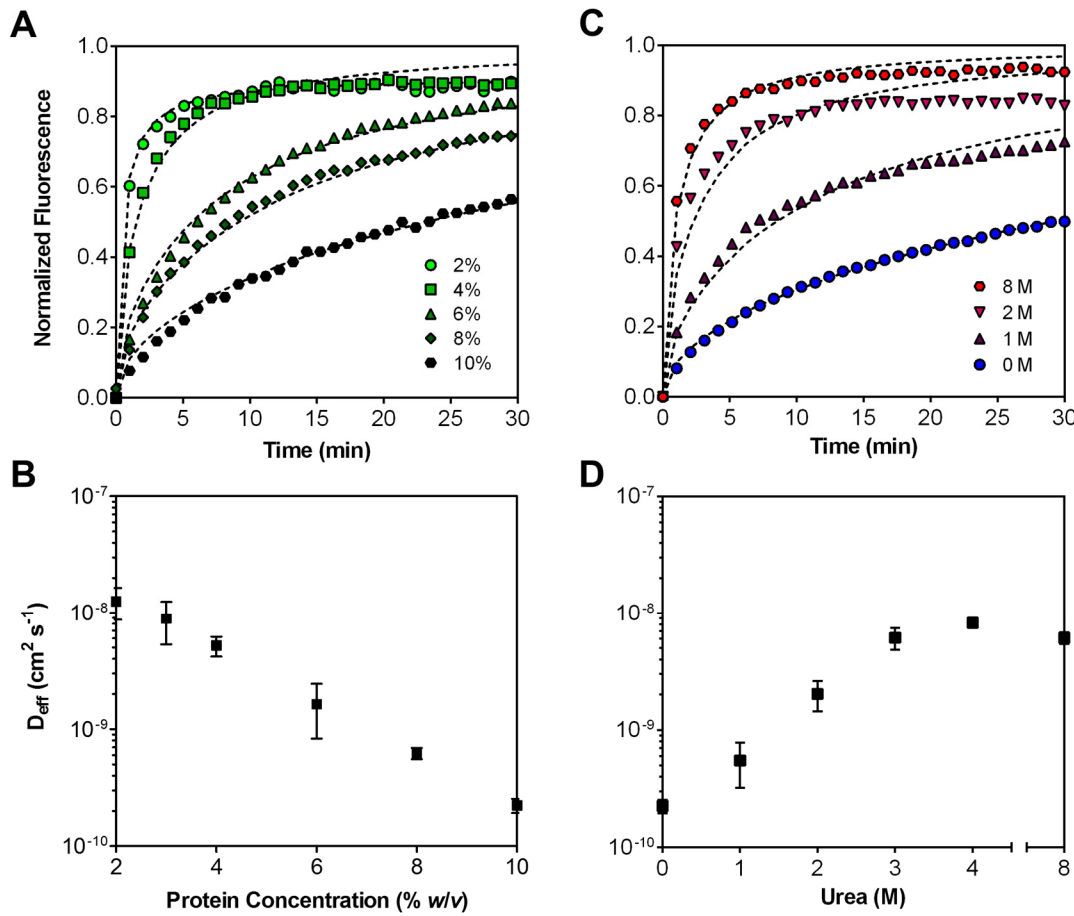


Figure 1.2. Quantitative analysis of chain mobility. The rate of fluorescence recovery after photobleaching in PEP hydrogels depends on gel density and concentration of denaturant. (A) FRAP curves generated from gels prepared at protein concentrations ranging from 2% to 10%, showing that the recovery rate decreases with increasing gel density. (B) Quantification of effective chain mobility as a function of gel density. D_{eff} varies inversely with gel density. (C) FRAP curves generated from 10% protein solutions prepared in increasing concentrations of urea. Fluorescence recovery rates increase with increasing amounts of urea, indicating disruption of interchain binding. (D) Quantification of the urea recovery curves. D_{eff} rises with increasing concentrations of urea, eventually reaching a plateau above 3 M. Error bars represent mean \pm standard deviation ($n \geq 3$ recovery curves from at least two gels). Dashed curves in A and B represent fits generated from the effective diffusion model.

urea are sufficient to inhibit association of the N- and C-terminal domains of PEP. Disruption of interchain binding destroys network integrity; samples prepared in high concentrations of urea (greater than 2 M) were viscous liquids.

1.4.3 3-state “hopping” model of chain migration in reversible hydrogels

Although the preceding analysis provides a useful description of chain mobility in PEP networks, it does not separate the effects of diffusion and interchain association. We sought to distinguish the roles of diffusion and binding in PEP networks. To this end, we formulated a model that captures both the diffusive and reactive elements of strand exchange in a physical molecular network. Our model is an extension of a 2-state reaction-diffusion model originally developed by Sprague et al., which relates the rate of fluorescence recovery to an equilibrium between two states: one free and one bound (18). Because each PEP chain has two terminal P domains, we chose to model network association as an equilibrium involving three sequential states (represented schematically in **Figure 1.3A**):



In the free state (*f*) neither P domain is bound to another and the chain can diffuse throughout the network with a self-diffusivity D_f . If both P domains on the chain join coiled-coil bundles, the chain enters the bound state (*b*) and becomes fully network-associated. We also consider an intermediate dangle state (*d*) in which only one of the P domains is tethered to the network. We distinguish the diffusion coefficient of free chains D_f from the effective diffusion coefficient D_{eff} , which represents diffusion slowed by binding. Because D_f represents free diffusion in the absence of binding, D_{eff} will be smaller than D_f whenever binding interactions

are significant. We now make several simplifying assumptions. First, we assume that both binding processes ($f \rightleftharpoons d$ and $d \rightleftharpoons b$) achieve equilibrium, and that both are governed by the same equilibrium constant ($K_1 \approx K_2 = k_{on}^*/k_{off}$). Note that $k_{on}^* = k_{on}S_{eq}$ is a pseudo-first-order rate constant calculated from the true association rate constant k_{on} (a second-order rate constant) by assuming a constant concentration of binding sites S_{eq} (18). We also assume that each P domain has a single binding mode, and that chain mobility in either of the two associated states (d or b) is negligible ($D_d = D_b \approx 0$). The physical picture is therefore one in which chains are constrained to migrate by “hopping” from site to site, but are otherwise fixed in space (**Figure 1.3B**). The distance a chain travels during such a transition (the “hopping radius”) is:

$$R^* = \sqrt{\frac{6D_f}{k_{on}^*}} \quad (\text{Eq. 2})$$

A material balance on **Eq. 1** results in a system of three coupled reaction-diffusion equations that can be used to model experimental FRAP curves and to estimate the three parameters in the model (k_{on}^* , k_{off} and D_f). We sought an analytical solution to the 3-state reaction-diffusion model. Following Sprague et al. for the 2-state model (18), Laplace transformation of **Eq. 1** yielded an analytical solution involving modified Bessel functions in Laplace space (see **Supporting Information** for details). When binding is neglected ($k_{on}^* \rightarrow 0$ and $k_{off} \rightarrow \infty$), the new solution reduces to the previously reported closed-form solution for free diffusion in a circular bleach spot (18, 30). Numerical inversion of the Laplace-domain solution using the MATLAB routine *invlap.m* produces the time-domain response (31), providing estimates

of model parameters by comparison with experimental curves. FRAP curves simulated using the 3-state model were fit to experimental curves using the MATLAB routine *nlinfit.m*, as well as a custom curve-fitting algorithm that gave comparable results (**Supplementary Figure 1.5**). With this approach, we found it difficult to obtain reliable estimates of all three model parameters from a single curve. Therefore, we simplified our curve-fitting procedure by first estimating D_f in a separate FRAP experiment using a non-binding elastin-like probe where the P domain endblocks were replaced by an irrelevant “A” peptide that does not form coiled-coils (see **Supplementary Table 1.1** for sequence) (32, 33).

Recovery rates observed with the non-binding “AECA” probe were 20- to 50-fold faster than those observed with the PECP probe (**Figure 1.3C** and **Supplementary Figure 1.6**). This provides further evidence that chain mobility is substantially reduced by reversible association of the coiled-coil domains. By attributing the recovery of AECA to diffusion alone, we estimated that D_f for an unbound PEP chain is approximately $1.59 \times 10^{-8} \text{ cm}^2 \text{ s}^{-1}$ in a 10% gel (assuming $D_f \sim M^{3/5}$ for a polymer chain in good solvent) (28). This value is similar to D_{eff} in dilute solutions of PEP (**Figure 1.2C**), and is within range of the diffusivities reported for macromolecules in other hydrogels. For example, dextran probes of similar molecular weight diffuse through dextran solutions and gels at approximately $10^{-7} \text{ cm}^2 \text{ s}^{-1}$, and unbound globular proteins diffuse through poly(ethylene glycol) gels at rates of $10^{-7} - 10^{-9} \text{ cm}^2 \text{ s}^{-1}$, depending on the hydrodynamic radius of the protein and the mesh size of the network (22, 28, 34 – 36).

Next we sought to estimate k_{on}^* and k_{off} for PECP. A grid of all possible (k_{on}^*, k_{off}) values was

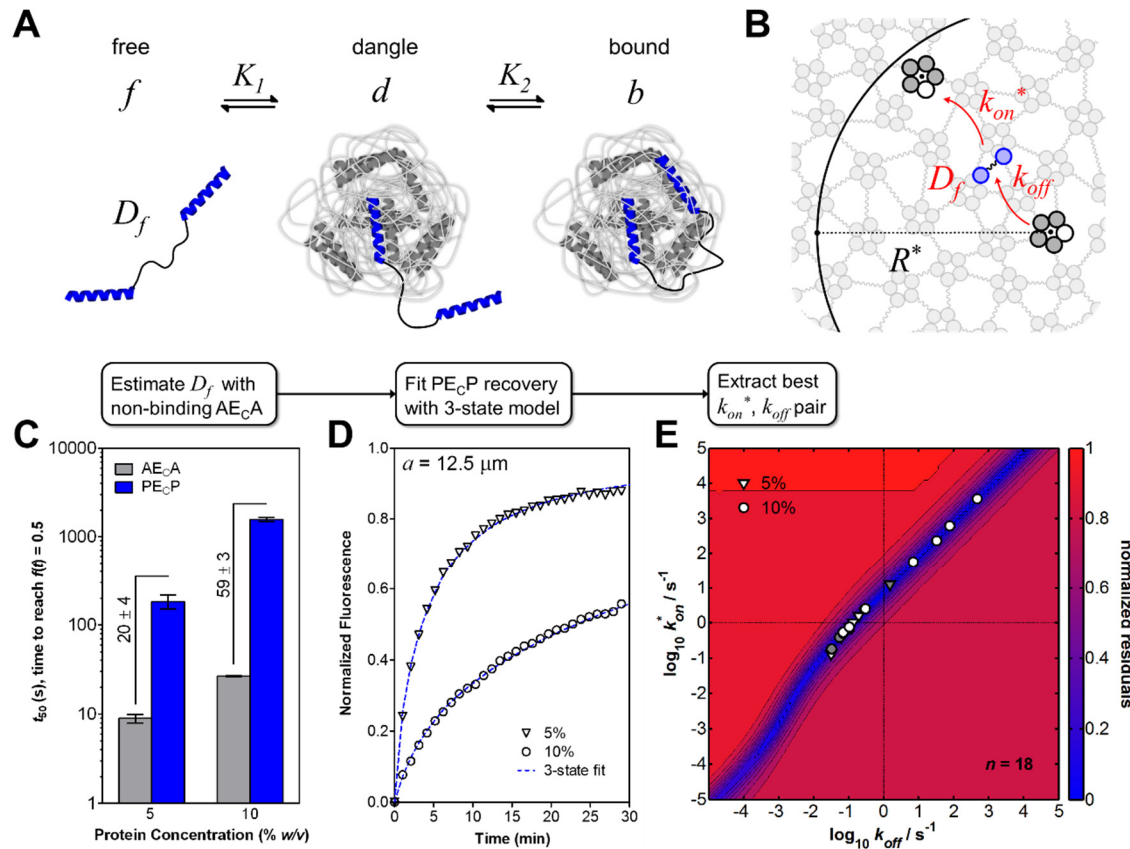


Figure 1.3. A 3-state reaction-diffusion analysis of chain migration in reversible hydrogels. (A) Illustration of the 3-state “hopping” model. **(B)** After a chain dissociates from an initial binding site (at a rate determined by k_{off}), it reassociates with a new junction at a rate determined by k_{on}^* . The average distance a free chain diffuses (“hops”) before rebinding is R^* . **(C)** AE_CA, a non-binding probe without terminal coiled-coils shows rapid fluorescence recovery compared to the associative probe PE_CP (vertical text shows fold-change \pm standard deviation, $n = 3$ recovery curves measured in one gel preparation for each probe). **(D)** The 3-state model yields excellent fits to the normalized recovery curves for a bleach spot radius (a) of $12.5 \mu\text{m}$. **(E)** Contour map showing normalized residuals of a representative 3-state model fit to a recovery curve from a 10% gel ($a = 12.5 \mu\text{m}$) for a wide range of k_{on}^* and k_{off} values. Points on the map represent (k_{on}^*, k_{off}) pairs obtained from independent photobleaching experiments performed in multiple gels ($a = 12.5 \mu\text{m}$, $n = 12$). Shaded symbols are experiments performed with a larger spot size ($a = 25 \mu\text{m}$, $n = 6$). The values of k_{on}^* obtained from 5% gels were multiplied by 2 in order to compare them with values from 10% gels on the same map.

sampled in log space (typically in increments of $10^{0.1}$ between 10^{-5} and 10^5 s) in order to find the pair that minimized the residuals between the simulated and experimental curves. This pair was then supplied as the initial guess in the MATLAB algorithm *nlinfit.m*, which finally produced a unique (k_{on}^*, k_{off}) pair corresponding to the best fit (18). Excellent fits to experimental FRAP curves were obtained with this procedure (**Figure 1.3D**). Within the range of bleach spot radii that we explored ($a = 1 - 25 \mu\text{m}$), the quality of the fit was relatively insensitive to the individual values of the rate constants, but strongly dependent on their ratio (**Figure 1.3E**). For a 10% gel and spot radius of $12.5 \mu\text{m}$, the data lie along a line with slope $k_{on}^*/k_{off} = 7.4 \pm 0.9$, whereas k_{on}^* itself ranges from 0.2 s^{-1} to $3.6 \times 10^3 \text{ s}^{-1}$.

To obtain estimates of the individual values of the rate constants, we made the assumption that k_{off} corresponds to the network relaxation rate measured by oscillatory shear rheometry (**Supplementary Figure 1.2**, $k_{off} \approx \omega_c$), and used the ratio of k_{on}^* to k_{off} to obtain k_{on}^* . This provides $k_{off} = 0.51 \pm 0.02 \text{ s}^{-1}$ and $k_{on}^* = 3.8 \pm 0.5 \text{ s}^{-1}$, suggesting a relatively weak binding equilibrium for the P domain. Strand exchange rates (k_{off}) reported for coiled-coils vary widely, e.g., $3 \times 10^{-3} \text{ s}^{-1}$ (GCN4) (37), $3 \times 10^{-4} \text{ s}^{-1} - 0.7 \text{ s}^{-1}$ (model leucine zippers) (16), 0.2 s^{-1} (Fos/Jun) (38), $1 \times 10^{-4} \text{ s}^{-1}$ (α -tropomyosin) (39), $6 \times 10^{-7} \text{ s}^{-1} - 5 \times 10^{-3} \text{ s}^{-1}$ (4-helix bundle proteins) (9, 40, 41). Refolding and association rates (k_{on}^*) are typically much faster (e.g., for Fos/Jun and GCN4, roughly 1 s^{-1} even at low μM concentrations, resulting in dissociation-limited exchange kinetics with K_d on the order of $0.01 - 1 \mu\text{M}$ for these zippers) (16, 38, 42). By comparison, all fits in **Figure 1.3E** give an average dissociation constant $K_d = 173 \pm 29 \mu\text{M}$. This leads to a free energy of network association $\Delta G_a = -5.1 \pm 0.1 \text{ kcal mol}^{-1}$. This number is within range of the Gibbs free energy of pentamer formation for native P ($\Delta G^\circ =$

-4.3 kcal mol⁻¹) estimated from thermal denaturation curves using circular dichroism spectroscopy, and is similar in magnitude to folding energies for other weakly associating coiled-coil structures (43, 44).

Sprague et al. showed that, for the 2-state reaction-diffusion model, the full model may be simplified to the single-parameter effective diffusion model (*i.e.*, D_{eff} alone gives good fits) whenever the dimensionless constant $k_{on}^* a^2/D_f$ is significantly greater than unity (18). This constraint ensures that binding is rapid relative to the characteristic diffusion time of the experiment. An important characteristic of this regime is that the rate of fluorescence recovery is insensitive to the individual values of k_{on}^* and k_{off} , and depends only on their ratio. Using the above estimates for k_{on}^* and D_f , we find that $k_{on}^* a^2/D_f \sim 10^2$ when $a = 12.5 \mu\text{m}$. This suggests that all of the FRAP experiments reported here lie in the effective diffusion regime. This explains the imprecision in the estimates of k_{on}^* and k_{off} derived from our FRAP experiments (**Figure 1.3E**), and our ability to generate good fits of our FRAP curves using D_{eff} alone (**Figure 1.2A**).

1.4.4 Predicting the hopping mobility with the 3-state model

Given that $k_{on}^* a^2/D_f \gg 1$ (see the above discussion), we can assume local equilibrium during the fluorescence recovery process. Under this assumption, it can be shown that for a chain with N associative domains (*i.e.*, for an “ $N+1$ ”-state hopping model, see **Supporting Information**), the ratio D_f/D_{eff} is given by

$$\frac{D_f}{D_{eff}} = 1 + K_1 + K_1 K_2 + \dots + \prod_{i=1}^N K_i \quad (\text{Eq. 3})$$

This allows us to predict the hopping mobility D_{eff} for a chain with any number of associative domains, provided D_f and the equilibrium constants are known. In the case of the 3-state model (**Eq. 3**, $N = 2$) if only one of the equilibrium constants is known, it is possible to make inferences about the relative magnitudes of K_1 and K_2 by comparing predictions from **Eq. 3** to experimental mobilities. We therefore designed a “PEc” probe that could associate with the network only once. The recovery curve of PEc should reflect the equilibrium between free and dangling chains, thus providing an independent measurement of K_1 . We also refined our estimates of D_f by measuring the recovery rate of a non-binding “Ec” probe comprising only the elastin-like midblock. As before, we assume $D_f \sim M^{3/5}$ in order to estimate D_f for the larger, associative probes.

The fluorescence recovery curves for these probes are shown in **Figure 1.4A**. From the Ec probe we estimated D_f for PEcP as $2.94 \pm 0.35 \times 10^{-8} \text{ cm}^2 \text{ s}^{-1}$. This is roughly 2-fold larger than the value estimated from the recovery rate of AEcA, and suggests a slight tendency for the A domain to self-associate. Fitting the PEc recovery with a 2-state model (**Eq. 3**, $N = 1$) provides $K_1 = 26.5 \pm 4.5$. Under the assumption that $K_1 = K_2$, this estimate can be applied directly to the 3-state model (**Eq. 3**, $N = 2$) in order to predict D_{eff} for PEcP. This approach substantially under-predicts the observed mobility (**Figure 1.4B**, $D_{obs} = 5.1 \times D_{pred}$). Moreover, fitting the PEcP recovery with a 3-state model without prior knowledge of K_1 (again assuming equivalence of K_1 and K_2) provides $K_1 = K_2 = 11.7 \pm 1.8$. These data are summarized in **Table 1.1**.

We hypothesized that the disparity in the values of K_1 obtained from the PEc and PEcP

probes might reflect a difference in the values of the equilibrium constants for sequential binding of the two P domains of PEcP (**Figure 1.3A**), with K_1 greater than K_2 . To test this hypothesis, we performed coarse-grained Brownian Dynamics simulations of gel-forming telechelic polymers (see **Supporting Information** for details). We used a Kremer-Grest bead-spring model with “sticky” beads at the chain ends interacting through an attractive Lennard-Jones potential (45). **Figure 1.4C** shows a representation of a gel comprised of chains with a length of 100 beads. The stickers cluster to form distinct network junctions, which we define as groups of neighboring stickers. By analogy to the 3-state model, we define the state of a simulated chain by specifying whether its stickers are both free from junctions (*f*) or both attached to junctions (*b*), or if only one sticker is bound (*d*). K_1 and K_2 are then obtained by computing the fraction of chains in each state.

We find that a majority of the chains in our simulation are fully bound ($[b]_{eq} = 0.86$, see also **Supplementary Figure 1.7**), in good agreement with the fraction of bound PEP chains estimated by FRAP (**Table 1.1**, $[b]_{eq} = 0.91$). Importantly, asymmetry in the two binding constants is apparent in the simulation, with $K_1 = 21.2$, $K_2 = 6.3$, and $K_1/K_2 = 3.4$. We can also isolate K_1 and K_2 from our FRAP data by assigning the k_{on}^*/k_{off} ratio obtained from PEc to K_1 , and then resolving the discrepancy between D_{pred} and D_{obs} for PEcP by treating K_2 as an adjustable parameter (**Eq. 3**). Interpreting the FRAP data in this way provides $K_1 = 26.5 \pm 4.5$, $K_2 = 6.0 \pm 2.1$, and $K_1/K_2 = 4.4 \pm 1.7$, in good agreement with the simulation. These observations are consistent with the hypothesis that reversible binding of a telechelic polymer to a macromolecular network is inherently asymmetric: the second binding event is disfavored relative to the first.

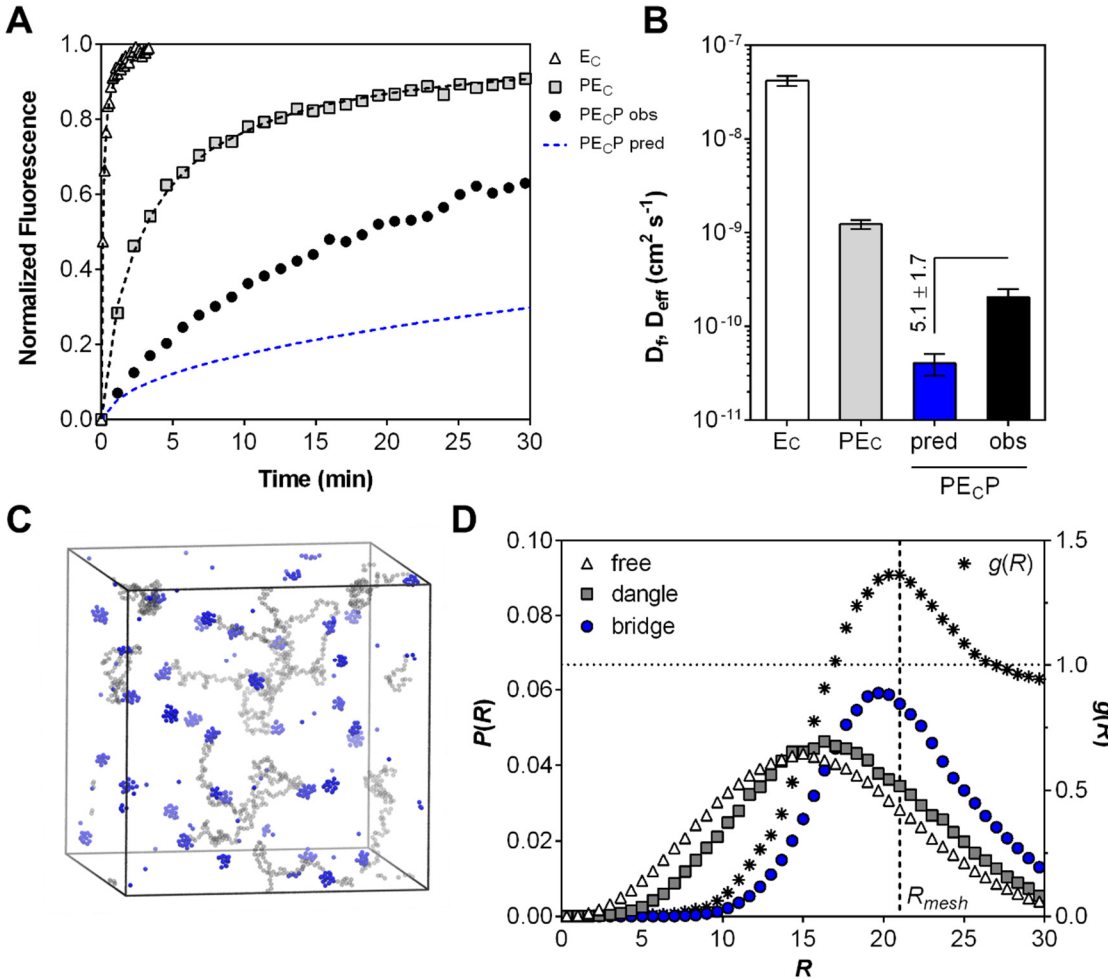


Figure 1.4. Predictions from the 3-state model imply binding asymmetry in PEP hydrogels. (A) FRAP experiments on E_C and PE_C probes provide independent estimates of D_f and K_1 that, together with Eq. (3), predict D_{eff} and the recovery rate of $PE_C P$ (blue dashed line). The experimentally observed recovery rate is higher than predicted, suggesting asymmetric sequential binding where $K_1 > K_2$. Fits to the E_C and PE_C curves were generated with 1-state (Eq. 3, $N = 0$) and 2-state (Eq. 3, $N = 1$) effective diffusion models, respectively (black dashed lines). (B) Assuming $K_1 = K_2$ under-predicts the observed D_{eff} for $PE_C P$ by roughly 5-fold (mean \pm SD, $n \geq 2$ gel preparations per probe). (C) Snapshot of a simulated gel with stickers (blue) connected by non-sticker beads (grey). The non-sticker beads of only 10 chains are shown for clarity. (D) Origin of the binding asymmetry. The radial distribution function of network junctions $g(R)$ is shown together with the chain end-to-end distributions $P(R)$ for the three states (bins of $\Delta R = 0.67$ were used in computing the distributions).

Free and dangling chains can adopt a substantial set of conformations at distances $R < R_{mesh}$, the location of maximum junction density. These conformations are lost upon entry into the bridge state.

We propose that the inequality of K_1 and K_2 arises from a difference in the entropic penalties associated with successive binding events. In transitioning from the free to the dangle state, a chain becomes restricted to a fraction of the system volume, and loses entropy in proportion to the change in accessible volume. The subsequent transition from dangle to bridge causes a similar entropic loss, but with the additional constraint that the volume accessible to the remaining chain end also depends on the junction spacing. Gelation promotes a depletion of neighboring junctions below the characteristic mesh size of the gel. Dangling chains must discard the rich set of conformations accessible below this length scale when they bridge neighboring junctions.

The effects of network structure on chain conformation are apparent in our simulation.

Figure 1.4D compares the distributions of chain end-to-end distances $P(R)$ for the three major states to $g(R)$, the junction radial distribution function. Free and dangling chains can access a substantial set of conformations at distances $R < R_{mesh}$, the location of maximum junction density. In contrast, bridged chains are restricted to a narrower set of end-to-end distances that correspond closely to R_{mesh} . Mild chain stretching in the bridged state is also apparent, which may enhance the degree of binding asymmetry we observe (the average end-to-end distance of bridged chains R_b exceeds that of dangling chains R_d by a factor of 1.2). However, substantial conformational freedom may still be lost in transition from dangle to bridge, even in the absence of chain stretching.

An intriguing possibility is that, in addition to hopping, the diffusivity of a PEcP probe may be enhanced by “walking”; *i.e.*, by cycling between the dangle and bound states d and b . In this process, the chain migrates through the network in discrete steps that correspond to the average distance between binding sites. A simple scaling analysis argues that this diffusive mode is not significant in PEP gels. Consider a chain with both ends bound to the network. The characteristic diffusivity of this chain can be estimated as $D_b \sim R_b^2/\tau_b$, where $\tau_b \approx k_{off}^{-1}$ is the average lifetime of the bound state. The expected contribution of this state to D_{eff} is $[b]_{eq}D_b$. As before, we obtain k_{on}^* and k_{off} for each state by setting k_{off} equal to the relaxation rate obtained from rheometry (**Supplementary Figure 1.2**), then using the k_{on}^*/k_{off} ratios calculated from FRAP (**Table 1.1**). Independent estimates of R_b from Flory theory ($R \sim bN^{3/5}$) (28), light-scattering measurements on unstructured amino acid midblocks (46), and a geometric argument based on binding site density suggest $R_b = 7.8 - 13.7$ nm for an ideal PEP network. These estimates provide $[b]_{eq}D_b \approx 0.0023D_{eff}$ for bound chains and $[d]_{eq}D_d \approx 0.0029D_{eff}$ for dangling chains, whereas $[f]_{eq}D_f \approx 1.00D_{eff}$. Other modes of bound mobility, including diffusion of chains in large-scale clusters, are excluded by a similar analysis.

We can appreciate why hopping dominates the mobility of PEP chains by considering the hopping radius R^* in relation to $R_b \approx R_{mesh}$. From **Eq. 2** we estimate that the average distance of a hop is $R^* = 1100 \pm 240$ nm, roughly 100-fold larger than R_{mesh} . Hence an escaped chain can diffuse many times its own length (past multiple potential binding sites) before rebinding. This result is consistent with a conceptual picture of a network linked together through well-formed coiled-coil junctions, in which most potential binding sites are fully occupied. Recently, Tang et al. invoked a non-zero bound state mobility in order to explain anomalous

self-diffusion behavior observed by forced Rayleigh scattering (FRS) in a reversible protein hydrogel assembled from chains with four coiled-coil P blocks per chain (47). Bound mobility (possibly in the form of large clusters) is likely to be more significant in these gels, due to the much smaller fraction of free chains.

1.4.5 Tuning chain mobility with protein engineering

Reversible network association of the P domain reduces the effective diffusivity of PEP chains by two orders of magnitude. Given the programmability of coiled-coil assembly (48), we imagined that it should be possible to control the effective diffusivity of a PEP chain by tuning the binding affinity of the P domain. In solution, coiled-coil assembly is driven by hydrophobic interactions between P domains (43). In the pentameric bundle, 48% of the total solvent-accessible area arising from the five individual helices is buried, demonstrating the critical role played by hydrophobic interactions in stabilizing the pentamer (27). We hypothesized that the hydrophobic leucine (Leu) contacts known to direct oligomerization of the P domain are also critical for reversible network association of a PEP chain.

Site-directed mutagenesis was performed on both ends of the original PEcP probe to examine whether replacement of critical Leu residues would increase chain mobility. Guided by previous mutagenesis studies on the P domain (43), we made a single Leu → Ala mutation (L37A) within each terminal coil, which we predicted would reduce the thermodynamic driving force for oligomerization of the probe. L37 occupies the *a*-position of one of the heptad repeats of P (**Figure 1.5A**). Residues at the *a*-positions line the hydrophobic interior of the pentameric helical bundle, and their mutation to Ala destabilizes the assembly (43).

We observed more rapid fluorescence recovery in PEP networks labeled with PEcP-L37A as compared to unmodified PEcP (**Figure 1.5A**). We attribute the faster recovery behavior to a reduction in the strength of association of the mutant probe with network junctions, consistent with the previously reported low helicity and monomeric oligomerization state of P domains carrying the L37A mutation (43).

The enhanced mobility of the PEcP-L37A probe illustrates the importance of hydrophobic interactions in network assembly, and suggests that increasing the hydrophobic character of the P domain should reduce chain mobility by increasing the strength of network association. We previously reported that replacement of Leu by (2S,4S)-2-amino-4-methylhexanoic acid (homoisoleucine, Hil), a leucine surrogate with expanded hydrophobic surface area, significantly increases the thermostability of dimeric coiled-coil assemblies (49). We hypothesized that replacement of the Leu residues in PEcP by Hil (**Figure 1.5A**) might reduce probe mobility.

To test this hypothesis, we prepared PEcP-Hil probes in which ca. 92% of all Leu residues were replaced by Hil (see **Supplementary Figures 1.8, 1.9** and **Supplementary Table 1.2** for details). In contrast to the accelerated recovery behavior of the PEcP-L37A mutant probe, recovery of the PEcP-Hil probe was slower than that of PEcP (**Figure 1.5B**). Moreover, probes containing both Hil and Leu exhibited intermediate rates of recovery (ca. 53% replacement, **Supplementary Figure 1.10**). This confirms that the reduced rate of fluorescence recovery derives from a differential association of the PEcP-Hil probes with the PEP network junctions.

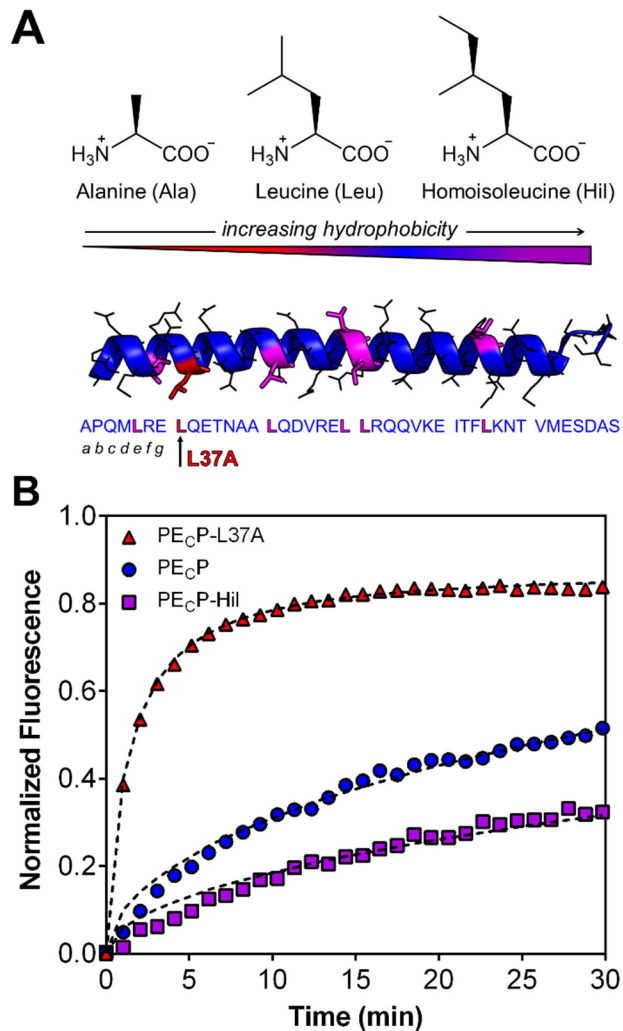


Figure 1.5. Genetic manipulation of the P domain controls the effective mobility of PE_cP probes. (A) PyMOL rendering of a single P domain α -helix showing the location of key Leu residues (purple). An Ala mutation at position 37 (red) is known to destabilize binding, and was predicted to increase probe mobility. Global replacement of Leu with the non-canonical amino acid Hil was predicted to increase the hydrophobic surface area of the probe and decrease its mobility. (B) FRAP of the engineered probes. PE_cP-L37A shows accelerated fluorescence recovery relative to PE_cP, whereas PE_cP-Hil shows slower recovery. Dashed lines depict fits generated from the effective diffusion model.

Table 1.1. Summary of FRAP results determined from engineered probes in 10% PEP hydrogels. Values represent mean \pm standard deviation ($a = 10 - 12.5 \mu\text{m}$, $n \geq 4$ recovery curves from at least two gel preparations per probe). Results for the PE_C probe are determined from the 2-state model (Eq. 3, $N = 1$); k_{on}^*/k_{off} for this probe reflects K_1 . Results for PE_CP-type probes are calculated from the 3-state model (Eq. 3, $N = 2$) with $D_f = 2.9 \pm 0.4 \times 10^{-8} \text{ cm}^2 \text{ s}^{-1}$, and assuming $K_1 = K_2 = k_{on}^*/k_{off}$.

Probe	M_w (kDa)	D_f, D_{eff} ($10^{-10} \text{ cm}^2 \text{ s}^{-1}$)	k_{on}^*/k_{off}	$[f]_{eq}$	$[b]_{eq}$	K_d (μM)	ΔG_a (kcal mol ⁻¹)
AE _C A	20.9	270 ± 190	-	1.000	-	-	-
E _C	17.7	420 ± 50	-	1.000	-	-	-
PE _C	25.4	12.3 ± 1.4	26.5 ± 4.5	0.036	-	47 ± 5	-5.9 ± 0.1
PE _C P <i>pred</i>	32.2	0.4 ± 0.1	26.5 ± 4.5	-	-	-	-
PE _C P <i>obs</i>	32.2	2.1 ± 0.5	11.7 ± 1.8	0.007	0.914	108 ± 13	-5.4 ± 0.1
PE _C P-L37A	32.1	51 ± 17	1.9 ± 0.7	0.174	0.531	720 ± 190	-4.3 ± 0.2
PE _C P-Hil	32.4	0.68 ± 0.09	20.3 ± 1.4	0.002	0.951	62 ± 4	-5.7 ± 0.04

1.5 Conclusion

We have reported a FRAP-based method for characterizing strand exchange and polymer self-diffusivity in associative protein hydrogels. The application of this method relies on a novel 3-state reaction-diffusion model of the strand exchange process. In this model, polymer chains move by a process called “hopping”: the chains are free to diffuse spatially throughout the polymer network, unless trapped by reversible association with network junctions. This model fits our experimental FRAP curves well, and permits extraction of diffusion coefficients and equilibrium constants. We find that reversible network association exerts significant control over the effective mobility of individual chains. This allows the effective

mobility “ D_{eff} ” to be tuned over a 500-fold range for probes that are all nominally the same size (**Table 1.1**), via simple changes in chain sequence. The formalism of the 3-state model also enables explicit prediction of D_{eff} from an underlying knowledge of the binding strength k_{on}^*/k_{off} and the free diffusivity D_f . The hopping mobility predicted by this formalism significantly underestimates the observed mobility. We interpret this discrepancy as indicating inequality of the equilibrium constants that control sequential binding to the network. Brownian Dynamics simulations support this interpretation, and suggest that the asymmetry in binding arises from an entropic constraint on the association of dangling chains due to local network structure. Importantly, such binding asymmetry is likely to be a general feature of reversible gels. Rigorous testing of this hypothesis is described in Chapter 2. Taken together, our results demonstrate that FRAP is well-suited to probing diffusion and binding in protein hydrogels, and that facile protein engineering techniques afford a remarkable level of control over chain mobility in these systems.

1.6 Acknowledgments

We thank Steven Olsen and the Division of Chemistry and Chemical Engineering Instrument Shop for machining sample holders for the FRAP experiments. We also thank David Koos, Andres Collazo and the Biological Imaging Facility of the Caltech Beckman Institute for training and assistance in operating the confocal microscope. We thank John Bagert, Lawrence Dooling, and Cole DeForest for helpful discussions during the preparation of the chapter.

1.7 Supporting Information

1.7.1 Materials and Methods

Plasmids. PEP was encoded on a pET15b vector (50). Insertion mutagenesis was performed on pET-15b-PEP at the center of the elastin-like midblock to yield pET15b-PEcP, i.e. PEP with a cysteine in the elastin domain. To construct the PEcP-L37A mutant, site-directed mutagenesis was performed on both “L37” residues in pQE15b-PEcP using “QuikChange” mismatch primers amplified by PfuUltraII HS Fusion Polymerase (Agilent Technologies). The L37A mutations in both P blocks were confirmed by forward and reverse sequencing, and by MALDI-MS on trypsinized PEcP-L37A. Incorporation of homoisoleucine (Hil) was achieved by placing PEcP into a modified pQE80L vector (pQE80L-LeuRS), containing a copy of the *leuRS* gene flanked by *NheI* sites downstream of the multiple-cloning site in pQE-80L. The pQE80L-LeuRS vector drives constitutive overexpression of leucyl-tRNA synthetase. Protein PEc encoded in pQE-80L was the kind gift of Larry Dooling. AEcA was the kind gift of Dr. Wenbin Zhang, and Ec was prepared by QuikChange mutagenesis on a pQE80L plasmid encoding the E domain only. All plasmids used and their corresponding coding sequences are presented in **Supplementary Table 1.1.**

Protein Expression and Purification. Plasmids coding for the proteins of interest were transformed into either BL21 (DE3) competent *E. coli* or the leucine auxotroph DH10B (for Hil incorporation). In order to express the polymers, cells transformed with the relevant vectors were cultured overnight, and the overnight cultures (typically 10 mL) were used to

inoculate 1 L flasks containing Terrific Broth (TB) supplemented with 100 – 200 mg ml⁻¹ ampicillin. Cells were grown to an OD₆₀₀ of 0.7 – 1.0 and then induced with 1 mM isopropyl β -D-1 thiogalactopyranoside (IPTG). After 4-5 h, bacterial cultures were harvested by centrifugation for 5-10 min at 10,000g, and cells were lysed with 8 M urea. Cell lysates were freeze-thawed at least once before being subjected to high-power tip sonication for homogenization (50 mL of lysate from a 1 L culture was typically treated with 30-50 W for 10 min in 0.5 - 1 s pulses). Homogenized lysate was clarified by high-speed centrifugation (30,000g for 1 h) and then subjected to standard His-tag purification over Ni-NTA agarose beads (Qiagen). His-purified lysate was dialyzed against 4 L of distilled water at 4 °C. The water was changed repeatedly (5-6 times) over the course of several days. Typically the onset of cloudiness inside the dialysis bag was used as the dialysis endpoint, after which point the aqueous suspensions were lyophilized.

Synthesis of homoisoleucine (Hil, 2-amino-4-methylhexanoic acid, CAS 3570-21-6) was performed following a previously reported procedure (49). For expression of proteins containing Hil, we performed a medium-shift with the *E. coli* leucine auxotroph DH10B into Leu-depleted medium supplemented with Hil. Hil is activated by the *E. coli* leucyl-tRNA synthetase (LeuRS) at lower rates than Leu (49). In order to achieve high levels of substitution, we prepared a new expression cassette that encoded a constitutively expressed copy of LeuRS downstream of an inducible PE_CP gene (**Supplementary Figure 1.8**). This pQE-80L-PE_CP-LeuRS plasmid enabled high levels of LeuRS expression when transformed into the *E. coli* leucine auxotroph DH10B. Expression of PE_CP was then induced from this plasmid in minimal media supplemented with different ratios of Hil to

Leu. Single colonies of DH10B transformed with pQE-80L-PEcP-LeuRS were used to inoculate 5 mL overnight cultures of M9 minimal medium containing glucose (0.4% w/v), thiamine HCl (35 mg L⁻¹), 1 mM MgSO₄, 0.1 mM CaCl₂, and all 20 amino acids (40 mg L⁻¹) supplemented with 200 mg L⁻¹ ampicillin. In large-scale (1 L) expressions, overnight cultures were inoculated into fresh M9 + 20 AA media and grown with agitation at 37 °C until the OD₆₀₀ reached 0.8 – 1.0. Cells were pelleted at 6,000g for 5-10 min at 4 °C, washed 3 times in ice-cold NaCl (0.9% w/v) and resuspended in fresh M9 media containing 500 μM of (2S,4S)-Hil with or without Leu. Cultures were then shaken at 37 °C for 15 min before induction with 1 mM IPTG. After 5 h, cells were harvested and the proteins purified as described above. The extent of replacement of Leu by Hil was estimated by MALDI mass spectrometry (**Supplementary Figure 1.9** and **Supplementary Table 1.2**). For PEcP expressed in Leu-depleted medium supplemented with 500 μM Hil, the extent of replacement was ca. 92%. The replacement level was reduced to 53% by including 100 μM Leu in the expression culture (see column “Leu + Hil” in **Supplementary Table 1.2**).

Labeling of Probes with Fluorescein-5-Maleimide. Fluorescent hydrogels were prepared by adding low concentrations of a fluorescently labeled PEP analogue to normal PEP networks. For example, PEP containing a single cysteine residue in its elastin-like midblock (PEcP) was site-specifically conjugated to fluorescein. For conjugation, 100 μM PEcP was typically dissolved in 8 M urea, pH 7.5 – 8, supplemented with 100 mM NaH₂PO₄. Tris-(2-Carboxyethyl)phosphine Hydrochloride (TCEP, ThermoFisher Scientific) was added to a final concentration of 2 mM, giving a 20:1 ratio of reducing agent to protein. This solution was reduced for 30 min before addition of fluorescein-5-

maleimide (*f5m*, Pierce) to a final concentration of 1 mM. Fluorophore was incubated with protein for 2 – 4 h at room temperature in order to label free thiols. Afterward, iodoacetamide (IAM) was added to a final concentration of 2 mM to alkylate remaining thiols. Alkylation with IAM was typically performed overnight at 4 °C. Labeled polymer was separated from unreacted dye by purification over Ni-NTA agarose. The extent of polymer labeling was estimated to be roughly 0.5 moles label per mole of polymer based on absorption measurements at 488 nm and comparison to free fluorescein-5-maleimide in a solution of dilute (1% *v/v*) 2-mercaptoethanol. A small amount of PEcP-*f5m* was mixed with solutions of unlabeled PEP. Solutions with PEcP:PEP mass ratios of 1:50 or 1:100 were typically prepared. These solutions were dialyzed against distilled water and lyophilized. Similar to unlabeled networks, addition of phosphate buffer to lyophilized protein containing fluorescent PEcP-*f5m* resulted in optically clear, fluorescent hydrogels after several hours on ice.

Rheological Measurements. Oscillatory shear rheometry was conducted on labeled and unlabeled PEP hydrogels using an ARES-RFS strain-controlled rheometer (TA Instruments) equipped with parallel-plate and cone-and-plate geometries. The outer edge of the plate was coated with mineral oil to minimize evaporation. Sample temperature was maintained at 25 °C. Strain sweeps identified a linear regime between 0.1 and 10% strain at 10 rad s⁻¹. Frequency sweeps were performed at a fixed strain amplitude of 1% between 0.1 and 100 rad s⁻¹.

Fluorescence Recovery After Photobleaching. After retrieval of the raw fluorescence recovery data from the Zen 2009 software, the data were typically normalized using two separate transformations. The following function normalizes the recovery curve to a range of [0, 1]:

$$f(t) = \frac{F(t)/F_\infty(t)}{F(t_0)/F_\infty(t_0)}$$

Following this first normalization, the data were typically scaled such that $f(t_0) = 0$ in order to enable fitting of the experimental curves to the simulated curves (which all begin at $f=0$). This scaling was accomplished using

$$\bar{f}(t) = \frac{f(t) - \min[f(t)]}{\max[f(t)] - \min[f(t)]}$$

In some instances, the experimental curve given by scaled $f(t)$ appeared to not be recovering to its maximum value of 1, even after long times. This may be due to a small fraction of immobile probes in the network. In instances where full recovery was not observed, the simulated fluorescence recovery (generated by the model) was sometimes multiplied by a scalar constant m representing the total fraction of mobile network chains in order to produce better fits to the data. In cases where this “mobile fraction” fit was required, m was typically found to be between 0.8 and 1.0 (i.e. less than 20% of the chains were treated as immobile).

In experiments with the non-binding probes (AECA and Ec), we frequently observed normalized fluorescence recovery values that moderately exceeded the pre-bleach spot

intensity (see **Supplementary Figure 1.6** below for an example). In these cases, the [min, max] scaling above was essential for properly experimental modeling.

1.7.2 Simulation Details

To explore possible binding asymmetry (differences between K_1 and K_2), we performed coarse-grained Brownian Dynamics simulations of gel-forming telechelic polymers. As described above, we used a standard Kremer-Grest model with beads at the ends of the chains (“stickers”) interacting through a Lennard-Jones (LJ) potential that was truncated and shifted to zero at $2.5\sigma_{LJ}$ (such that the stickers experience the attractive portion of the potential) and assigned a well depth of ϵ_s (45). The LJ potential for all other bead pairs was truncated and shifted at $2^{1/6}\sigma_{LJ}$ (such that the potential is purely repulsive) and assigned a well depth of $\epsilon = kT$ (where kT is the thermal energy). All lengths are expressed in units of the LJ diameter σ_{LJ} which we set to unity. The chain connectivity is described with a FENE potential using a spring constant of $k = 30$ and a fully stretched bond length of $R_0 = 1.5$ (both of which are expressed in terms of reduced LJ units $\epsilon = \sigma_{LJ} = 1$). We used a system box size of $V = L^3$ with $L = 4.1R_f$, where $R_f \approx 15.3$ is the equilibrium end-to-end distance of free chains. We imposed periodic boundary conditions in all directions. The bead number density was $\rho = 0.12$, ensuring that the solution is semi-dilute ($\rho \approx 1.6\rho^*$, where ρ^* is the overlap concentration).

We used Langevin dynamics to evolve the system:

$$m\ddot{r} = f_p + f_b - \zeta\dot{r}$$

where r and f_p are, respectively, the particle position and interparticle force, and the particle mass m is set at unity. The damping coefficient was set to $\zeta = 1$ to ensure overdamped dynamics. The Brownian force f_b was taken to be white noise with a mean of 0 and a variance of $2kT\zeta$. We integrated using a timestep of $\delta t = 0.003$. To reach the equilibrium state for $\epsilon_e = 4.5$, the sample was annealed at a temperature of $kT = 4.5$ for a duration of $2\tau_R$ (where τ_R is the Rouse time of the system), followed by quenching to $kT = 1$ over a period of $5\tau_R$. We then further equilibrated each sample for $5\tau_R$. The data (e.g. state fractions, $P(R)$, and $g(R)$) were then collected over a period of $20\tau_R$.

To characterize the state of a chain (e.g. free, bound, etc.) we must first define the junctions of the gel. We define junctions as groups of two or more associating stickers. Stickers within a cutoff distance of 1.5 (capturing the attractive portion of the LJ potential-well) are deemed associating and grouped into the same junction.

1.7.3 Derivation of the analytical solution to the 3-state model

The 3-state reaction-diffusion model of strand exchange considers three sequential states in equilibrium that describe the process of network association for PEP chains:



In this model, the free chain f must undergo two separate association events in order to become fully bound b or network associated. An intermediate dangle state d appears in which only one of the two P domains participates in a network junction. This situation is depicted graphically in **Figure 1.3** and **Supplementary Figure 1.3**. Sprague et al.

developed a FRAP model for analyzing probe diffusion when the probe itself undergoes a single binding reaction (2-state), or two independent binding reactions with structurally unrelated binding sites (alternative 3-state) (18). We sought to extend their analysis of a 2-state system to a 3-state system with sequential binding reactions. The analysis below closely follows their development of an analytical solution for the 2-state system (see especially their Appendix). In our case, a material balance on (Eq. S1) results in the following system of coupled reaction-diffusion equations, where $[A]$ denotes the molar concentration of a given species A :

$$\begin{aligned}\frac{\partial[f]}{\partial t} &= D_f \nabla^2[f] - k_{on}^*[f] + k_{off}[d] \\ \frac{\partial[b]}{\partial t} &= k_{on}^*[d] - k_{off}[b] \\ \frac{\partial[d]}{\partial t} &= k_{on}^*[f] - (k_{off} + k_{on}^*)[d] + k_{off}[b]\end{aligned}\quad (\text{Eq. S2})$$

Here we use are using the pseudo-first-order rate constant k_{on}^* , which is equal to the true second-order rate constant k_{on} , multiplied by the equilibrium molar concentration of binding sites $[S]_{eq}$ (see Eq. S26 and S27 below). Immediately following a photobleach, visible fluorophore is depleted in all three states within a cylinder of radius a that extends through the entire sample. Outside the radius of this cylinder, visible fluorophore remains at its equilibrium concentration. Because the photobleach is symmetric along the z -axis of the cylinder, only lateral diffusion in a single 2D plane needs to be considered. The initial conditions are:

$$\begin{aligned}
 f(r, t_0) &= \begin{cases} 0 & r \leq a \\ [f]_{eq} & r > a \end{cases} \\
 b(r, t_0) &= \begin{cases} 0 & r \leq a \\ [b]_{eq} & r > a \end{cases} \\
 d(r, t_0) &= \begin{cases} 0 & r \leq a \\ [d]_{eq} & r > a \end{cases}
 \end{aligned} \tag{Eq. S3}$$

It is convenient to normalize the equilibrium concentrations of each species with the requirement

$$[f]_{eq} + [d]_{eq} + [b]_{eq} = 1 \tag{Eq. S4}$$

At equilibrium, the concentration of each species may be found using the steady-state condition

$$\frac{\partial [f]}{\partial t} = \frac{\partial [d]}{\partial t} = \frac{\partial [b]}{\partial t} = 0$$

Applying this condition to (Eq. S2) together with (Eq. S4) results in the following relations for the equilibrium concentration of each species:

$$\begin{aligned}
 \frac{1}{[f]_{eq}} &= 1 + \left(\frac{k_{on}^*}{k_{off}} \right) + \left(\frac{k_{on}^*}{k_{off}} \right)^2 \\
 \frac{1}{[d]_{eq}} &= 1 + \left(\frac{k_{off}^*}{k_{on}} \right) + \left(\frac{k_{off}^*}{k_{on}} \right)^2
 \end{aligned} \tag{Eq. S5}$$

$$\frac{1}{[b]_{eq}} = 1 + \left(\frac{k_{off}}{k_{on}^*} \right) + \left(\frac{k_{off}}{k_{on}^*} \right)^2$$

We can also define a pseudo equilibrium constant K_{eq} as the ratio of gel-bound/free chains, which from the steady-state assumption can be shown to be:

$$K_{eq} = \frac{[b]_{eq}}{[f]_{eq}} = \left(\frac{k_{on}^*}{k_{off}} \right)^2 \quad (\text{Eq. S6})$$

It is convenient to make the following variable transformations:

$$\begin{aligned} u &= [f]_{eq} - f \\ v &= [b]_{eq} - b \\ w &= [d]_{eq} - d \end{aligned} \quad (\text{Eq. S7})$$

Using (Eq. S7), we can transform the system of equations in (Eq. S2) as follows.

$$\begin{aligned} \frac{\partial u}{\partial t} &= D_f \nabla^2 u - k_{on}^* u + k_{off} w \\ \frac{\partial v}{\partial t} &= k_{on}^* w - k_{off} v \\ \frac{\partial w}{\partial t} &= k_{on}^* u - (k_{on}^* + k_{off}) w + k_{off} v \end{aligned} \quad (\text{Eq. S8})$$

Furthermore, the initial conditions in (Eq. S3) now become

$$\begin{aligned}
 u(r, t_0) &= \begin{cases} [f]_{eq} & r \leq a \\ 0 & r > a \end{cases} \\
 v(r, t_0) &= \begin{cases} [b]_{eq} & r \leq a \\ 0 & r > a \end{cases} \\
 w(r, t_0) &= \begin{cases} [d]_{eq} & r \leq a \\ 0 & r > a \end{cases}
 \end{aligned} \tag{Eq. S9}$$

With this change of variables, we are now in a position to apply the Laplace transformation to the system in (Eq. S8). This transformation is given by

$$F(s) = L\{f(t)\}(s) = \int_0^\infty e^{-st} f(t) dt$$

After transformation into Laplace space, the new system of equations becomes:

$$s\bar{u} = D_f \nabla^2 \bar{u} - k_{on}^* \bar{u} + k_{off} \bar{w} + \bar{u}(0) \tag{Eq. S10}$$

$$s\bar{v} = k_{on}^* \bar{w} - k_{off} \bar{v} + \bar{v}(0) \tag{Eq. S11}$$

$$s\bar{w} = k_{on}^* \bar{u} - (k_{on}^* + k_{off}) \bar{w} + k_{off} \bar{v} + \bar{w}(0) \tag{Eq. S12}$$

Here \bar{u} has been used to distinguish the Laplace-domain variable from the time-domain variable u . In order to solve this system, at least one of the above expressions needs to be written in terms of a single variable. This can be achieved with (Eq. S10) by expressing w in terms of u using (Eq. S11) and (Eq. S12). Towards this goal, (Eq. S11) is first used to solve for $v(s)$ in terms of w , which gives

$$\bar{v} = q_v(s) [k_{on}^* \bar{w} + \bar{v}(0)] \quad (\text{Eq. S13})$$

where

$$q_v(s) \equiv \frac{1}{s + k_{off}} \quad (\text{Eq. S14})$$

Next (Eq. S13) can be substituted into (Eq. S12) to get w in terms of u

$$\bar{w} = q_w(s) [k_{on}^* \bar{u} + k_{off} q_v \bar{v}(0) + \bar{w}(0)] \quad (\text{Eq. S15})$$

where

$$q_w(s) \equiv \frac{1}{s + k_{on}^* + k_{off} - k_{on}^* k_{off} q_v} \quad (\text{Eq. S16})$$

Finally, (Eq. S16) can be substituted into (Eq. S10) which yields a differential equation in terms of u only. This equation has the simplified form

$$\nabla^2 \bar{u} - q_u(s)^2 \bar{u} = \begin{cases} -V & r \leq a \\ 0 & r > a \end{cases} \quad (\text{Eq. S17})$$

where q_u and V are defined as

$$q_u(s)^2 \equiv \left(\frac{1}{D_f} \right) [s + k_{on}^* - k_{off} k_{on}^* q_w] \quad (\text{Eq. S18})$$

$$V \equiv \left(\frac{1}{D_f} \right) [(k_{off})^2 q_w q_v \bar{v}(0) + k_{off} q_w \bar{w}(0) + \bar{u}(0)] \quad (\text{Eq. S19})$$

Here a “nested function” approach has been used to simplify the forms of (Eq. S17 – S19). This conceals the underlying algebraic complexity of (Eq. S17). Despite this complexity, the equation has a known solution of the form

$$\bar{u}_1 = \frac{V}{q_u^2} - \alpha_1 I_0(q_u r), \quad r \leq a$$

$$\bar{u}_2 = \alpha_2 K_0(q_u r), \quad r > a$$

where I_0 and K_0 are modified Bessel functions of the first and second kind, respectively.

To determine the constants α_1 and α_2 , we require that u and its first derivative be continuous at the bleach spot boundary $r = a$. Using this continuity requirement and the Bessel function relationships $I_0' = I_1$ and $K_0' = -K_1$, we arrive at the following expression for α_1

$$\alpha_1 = \left(\frac{V}{q_u^2} \right) q_u a K_1(q_u a) \quad (\text{Eq. S20})$$

In the time domain, what is actually measured is the average fluorescence intensity of all three states within the circular spot, i.e.

$$\langle f(t, r) \rangle = \langle f + d + b \rangle = \langle [f]_{eq} - u + [d]_{eq} - w + [b]_{eq} - v \rangle = 1 - \langle u + v + w \rangle$$

The Laplace transformation of this profile is

$$F(s, r) = \frac{1}{s} - \langle \bar{u} \rangle - \langle \bar{v} \rangle - \langle \bar{w} \rangle \quad (\text{Eq. S21})$$

The only term that depends on r in (Eq. S21) is u , so it suffices to compute the average for u . This can be done with the integral:

$$\langle \bar{u}(s) \rangle = \frac{1}{\pi a^2} \int_0^{2\pi} d\theta \int_0^a \left[\frac{V}{q_u^2} - \alpha_1 I_0(q_u r) \right] r dr$$

$$\langle \bar{u}(s) \rangle = \left(\frac{V}{q_u^2} \right) [1 - 2K_1(q_u a)I_1(q_u a)]$$

(Eq. S22)

Finally, we can combine all the preceding expressions into the final form

$$F(s, r) = \frac{1}{s} - \langle \bar{u} \rangle - \bar{v} - \bar{w}$$

$$F(s, r) = \frac{1}{s} - \left[1 + k_{on}^* q_w + (k_{on}^*)^2 q_w q_v \right] \langle \bar{u}(s) \rangle - Q_{wv}(s)$$

(Eq. S23)

where

$$Q_{wv}(s) = [k_{off} q_w q_v + k_{off} k_{on}^* q_w q_v^2 + q_v] \bar{v}(0) + [k_{on}^* q_w q_v + q_w] \bar{w}(0)$$

(Eq. S24)

We now consider the case in which binding is negligible, i.e. when $k_{on}^* \rightarrow 0$ and $k_{off} \rightarrow \infty$. In this case, it is immediately apparent from (Eq. S14) and (Eq. S16) that q_v and q_w approach zero. A similar analysis of (Eq. S24) under the same constraint also leads to the conclusion that Q_{wv} approaches zero. Furthermore, q_u^2 and V approach s/D_f and $1/D_f$ respectively. These reductions greatly simplify (Eq. S23), which can now be written as

$$F(s, r) = \frac{1}{s} - \langle \bar{u}(s) \rangle = \frac{1}{s} - \frac{1}{s} [1 - 2K_1(q_u a)I_1(q_u a)] = \frac{2K_1(q_u a)I_1(q_u a)}{s}$$
(Eq. S25)

Sprague et al. show that this relation is identical to the relation obtained by Soumpasis for a chain diffusing freely in a circular bleach spot (18, 30). To further validate our solution, we compared curves obtained by inversion of (Eq. S23) with those obtained by numerical simulation of (Eq. S8) and (Eq. S9) using a finite-difference method. FRAP curves simulated analytically and numerically showed good agreement across multiple values of k_{on} , with only minor differences at long times which could be attributed to the finite mesh size used in the difference algorithm (**Supplementary Figure 1.4**).

As discussed in the main text, the parameter k_{on}^* is a pseudo-first-order association rate, calculated from the true (second-order) association rate k_{on} by assuming a constant concentration of binding sites S_{eq} . The true second-order association rate is:

$$k_{on} = \frac{k_{on}^*}{S_{eq}} \quad (\text{Eq. S26})$$

The maximum molar concentration of equilibrium binding sites can be calculated from the network mass density ρ by assuming that all P domains are active in pentameric bundle formation. In this ideal case, S_{eq} is given by the following relation, where M is the molar mass of a single PEP chain (~32 kDa, **Supplementary Table 1.1**).

$$S_{eq} = \frac{2}{5} \left(\frac{\rho}{M} \right) \quad (\text{Eq. S27})$$

Use of (Eq. S26) and (Eq. S27) also permits determination of the dissociation constant K_d , which is simply the ratio of k_{off} to k_{on} . With K_d it is possible to estimate the free energy of network association ΔG_a from the relation:

$$\Delta G_a = -RT \ln \left(\frac{1}{K_d} \right) \quad (\text{Eq. S28})$$

Sprague et al. use the following parameter to describe rate constant parameter space, which is helpful for determining whether fluorescence recovery is primarily governed by either diffusion or binding, or a combination of both.

$$\varphi^2 = \frac{k_{on}^* a^2}{D_f} \quad (\text{Eq. S29})$$

1.7.4 *invlap.m*: a MATLAB script for inverse Laplace transformation

The following algorithm may be used to numerically invert the Laplace domain solution in (Eq. S23) in order to obtain simulated fluorescence recovery curves in the time domain. The algorithm was originally written by Karl Hollenbeck and should be cited as shown below. The original web link to the algorithm is no longer active.

Hollenbeck, K. J. (1998) INVLAP.M: A MATLAB function for numerical inversion of Laplace transforms by the de Hoog algorithm.
http://www.mathworks.com/matlabcentral/answers/uploaded_files/1034/invlap.m

```
% INVLAP numerical inverse Laplace transform
%
% f = invlap(F, t, alpha, tol, P1,P2,P3,P4,P5,P6,P7,P8,P9);
%
% F      laplace-space function (string referring to an m-file),
%         must have form F(s, P1,..,P9), where s is the Laplace
% parameter,
%         and return column vector as result
% t      column vector of times for which real-space function values
% are
%         sought
% alpha  largest pole of F (default zero)
% tol    numerical tolerance of approaching pole (default 1e-9)
% P1-P9 optional parameters to be passed on to F
% f      vector of real-space values f(t)
```

```

%
% example: identity function in Laplace space:
%   function F = identity(s);                                % save these two lines
%     F = 1./(s.^2);                                         % ... as "identity.m"
%   invlap('identity', [1;2;3])                                % gives [1;2;3]
%
% algorithm: de Hoog et al's quotient difference method with
% accelerated
% convergence for the continued fraction expansion
% [de Hoog, F. R., Knight, J. H., and Stokes, A. N. (1982). An
improved
%   method for numerical inversion of Laplace transforms. S.I.A.M. J.
Sci.
%   and Stat. Comput., 3, 357-366.]
% Modification: The time vector is split in segments of equal magnitude
%   which are inverted individually. This gives a better overall
accuracy.

%
% details: de Hoog et al's algorithm f4 with modifications (T->2*T and
%   introduction of tol). Corrected error in formulation of z.
%
% Copyright: Karl Hollenbeck
%   Department of Hydrodynamics and Water Resources
%   Technical University of Denmark, DK-2800 Lyngby
%   email: karl@isv16.isva.dtu.dk
% 22 Nov 1996, MATLAB 5 version 27 Jun 1997 updated 1 Oct 1998
% IF YOU PUBLISH WORK BENEFITING FROM THIS M-FILE, PLEASE CITE IT AS:
%   Hollenbeck, K. J. (1998) INVLAP.M: A matlab function for numerical
%   inversion of Laplace transforms by the de Hoog algorithm,
%   http://www.isva.dtu.dk/staff/karl/invlap.htm

function f = invlap(F, t, alpha, tol, P1,P2,P3,P4,P5,P6,P7,P8,P9);

if nargin <= 2,
  alpha = 0;
elseif isempty(alpha),
  alpha = 0;
end
if nargin <= 3,
  tol = 1e-9;
elseif isempty(tol),
  tol = 1e-9;
end
f = [];

%
% split up t vector in pieces of same order of magnitude, invert one
piece
%
%   at a time. simultaneous inversion for times covering several orders
of
%   magnitudes gives inaccurate results for the small times.

allt = t;                                % save full times vector
logallt = log10(allt);

```

```

iminlogallt = floor(min(logallt));
imaxlogallt = ceil(max(logallt));
for ilogt = iminlogallt:imaxlogallt,      % loop through all pieces

    t = allt(find((logallt>=ilogt) & (logallt<(ilogt+1)))); 
    if ~isempty(t),                         % maybe no elements in that magnitude

        T = max(t)*2;
        gamma = alpha-log(tol)/(2*T);
        % NOTE: The correction alpha -> alpha-log(tol)/(2*T) is not in de
        Hoog's
        % paper, but in Mathematica's Mathsource (NLapInv.m)
        implementation of
        % inverse transforms
        nt = length(t);
        M = 20;
        run = [0:1:2*M]';      % so there are 2M+1 terms in Fourier series
        expansion

        % find F argument, call F with it, get 'a' coefficients in power
        series
        s = gamma + i*pi*run/T;
        command = ['a = ' F '(s)'];
        if nargin > 4,                      % pass on parameters
            for iarg = 1:nargin-4,
                command = [command ',P' int2str(iarg)];
            end
        end
        command = [command ');'];
        eval(command);
        a(1) = a(1)/2;                      % zero term is halved

        % build up e and q tables. superscript is now row index, subscript
        column
        % CAREFUL: paper uses null index, so all indeces are shifted by 1
        here
        e = zeros(2*M+1, M+1);
        q = zeros(2*M, M+1);                 % column 0 (here: 1) does not exist
        e(:,1) = zeros(2*M+1,1);
        q(:,2) = a(2:2*M+1,1)./a(1:2*M,1);
        for r = 2:M+1,                      % step through columns (called
        r...)
            e(1:2*(M-r+1)+1,r) = ...
            q(2:2*(M-r+1)+2,r) = q(1:2*(M-r+1)+1,r) + e(2:2*(M-r+1)+2,r-1);
            if r<M+1,                      % one column fewer for q
                rq = r+1;
                q(1:2*(M-rq+1)+2,rq) = ...
                q(2:2*(M-rq+1)+3,rq-1).*e(2:2*(M-rq+1)+3,rq-1)./e(1:2*(M-
                rq+1)+2,rq-1);
            end
        end

        % build up d vector (index shift: 1)

```

```

d = zeros(2*M+1,1);
d(1,1) = a(1,1);
d(2:2:2*M,1) = -q(1,2:M+1).'; % these 2 lines changed after niclas
d(3:2:2*M+1,1) = -e(1,2:M+1).'; % ...

% build up A and B vectors (index shift: 2)
% - now make into matrices, one row for each time
A = zeros(2*M+2,nt);
B = zeros(2*M+2,nt);
A(2,:) = d(1,1)*ones(1,nt);
B(1:2,:) = ones(2,nt);
z = exp(i*pi*t'/T); % row vector
% after niclas back to the paper (not: z = exp(-i*pi*t/T)) !!!
for n = 3:2*M+2,
    A(n,:) = A(n-1,:)+d(n-1,1)*ones(1,nt).*z.*A(n-2,:); % different index
    B(n,:) = B(n-1,:)+d(n-1,1)*ones(1,nt).*z.*B(n-2,:); % shift for d!
end

% double acceleration
h2M = .5 * ( ones(1,nt) + ( d(2*M,1)-d(2*M+1,1) )*ones(1,nt).*z );
R2Mz = -h2M.*ones(1,nt) - ...
(ones(1,nt)+d(2*M+1,1)*ones(1,nt).*z/(h2M).^2).^5;
A(2*M+2,:) = A(2*M+1,:)+R2Mz .* A(2*M,:);
B(2*M+2,:) = B(2*M+1,:)+R2Mz .* B(2*M,:);

% inversion, vectorized for times, make result a column vector
fpiece = ( 1/T * exp(gamma*t') .* real(A(2*M+2,:)./B(2*M+2,:)) )';
f = [f; fpiece]; % put pieces together

end % if not empty time piece

end % loop through time vector pieces

```

1.7.5 Fitting procedures for experimental FRAP curves

In order to fit simulated curves to experimental curves, the following curve fitting procedures were employed. For the effective diffusion model (**Figure 1.2**), the full model (**Eq. S23**) was used but with the values of k_{on}^* and k_{off} fixed at 10^{-5} s⁻¹ and 10^5 s⁻¹ respectively. This was found to be numerically equivalent to fitting the curves with the form derived by Soumpasis (30):

$$f(t) = \exp\left(\frac{-\tau_D}{2t}\right) \left[I_0\left(\frac{\tau_D}{2t}\right) + I_1\left(\frac{\tau_D}{2t}\right) \right] \quad (\text{Eq. S30})$$

where

$$\tau_D = \frac{a^2}{D_f}$$

As discussed by Sprague et al., both (Eq. S25) and (Eq. S30) are solutions to the simple diffusion equation without any binding. When used to fit curves influenced by binding (i.e., in the effective diffusion regime), the diffusivity resulting from the fit is D_{eff} . Curves were fit using the method described in the main text, as well as by the following custom algorithm which gave similar results: (i) a guess for the parameter of interest (D_{eff} , D_f , k_{on}^* , k_{off}) was drawn from a normal distribution (generated by the MATLAB command `randn`) having a mean and standard deviation equal to an initial seed guess, (ii) based on the guess, a new FRAP curve was simulated from (Eq. S23) and compared to the experimental curve, (iii) the guess was accepted if it lowered the root-mean-square residual of the fit relative to the previous guess, and (iv) the next guess was drawn from a new normal distribution having a mean and standard deviation equal to the value of the new best guess for the fitting parameter. This procedure was typically iterated 1000 times, after which point a very good fit had usually been obtained. For fits using the full model, D_f was fixed in an independent experiment (by modeling recovery curves of the Ec probe with the pure diffusion equation), and then guesses for k_{on}^* and k_{off} were simultaneously drawn from independent normal distributions with means and standard deviations equal to the value of the current guess for each rate constant. As with the fits for D_f alone, new guesses were accepted whenever they

lowered the root mean square residual of the fit, and this procedure was iterated 1000 times.

Examples of fits resulting from this approach are shown in **Supplementary Figure 1.5**.

1.7.6 Derivation of Equation 3

Consider a generalized version of (Eq. 1), in which there are N associative “sticky” domains and therefore $N+1$ total states (including the free state f). Assume that the f state has a free diffusivity given by D_f , and that the mobility of chains in each of the remaining N states is given by a single non-zero value designated D_b for “bound mobility”.



If binding is fast relative to the time it takes to diffuse across the bleach spot, then we can assume local, instantaneous chemical equilibrium at each time throughout the course of fluorescence recovery (51). Under this assumption, it is trivial to show that

$$[d_i] \approx \left(\frac{k_{on}^*}{k_{off}} \right) [f]$$

$$[d_{i+1}] \approx \left(\frac{k_{on}^*}{k_{off}} \right) [d_i] = \left(\frac{k_{on}^*}{k_{off}} \right)^2 [f]$$

⋮

$$[b_N] \approx \left(\frac{k_{on}^*}{k_{off}} \right) [d_{N-1}] = \left(\frac{k_{on}^*}{k_{off}} \right)^N [f]$$

or more generally that

$$[d_i] \approx \left(\frac{k_{on}^*}{k_{off}} \right)^i [f] \quad \text{for } i = 1 \dots N \quad (\text{Eq. S32})$$

Proceeding to write out the reaction-diffusion equations for each state and then summing them together (all reaction terms disappear during this operation) gives:

$$\frac{\partial [f]}{\partial t} + \frac{\partial [d_i]}{\partial t} + \frac{\partial [d_{i+1}]}{\partial t} + \dots + \frac{\partial [b_N]}{\partial t} = D_f \nabla^2 [f] + D_b (\nabla^2 [d_i] + \nabla^2 [d_{i+1}] + \dots + \nabla^2 [b_N])$$

Supplying (Eq. S32) into the above relation gives

$$\left[1 + \left(\frac{k_{on}^*}{k_{off}} \right) + \left(\frac{k_{on}^*}{k_{off}} \right)^2 + \dots + \left(\frac{k_{on}^*}{k_{off}} \right)^N \right] \frac{\partial [f]}{\partial t} = \left\{ D_f + D_b \left[\left(\frac{k_{on}^*}{k_{off}} \right) + \left(\frac{k_{on}^*}{k_{off}} \right)^2 + \dots + \left(\frac{k_{on}^*}{k_{off}} \right)^N \right] \right\} \nabla^2 [f]$$

Letting $\frac{k_{on}^*}{k_{off}} = \alpha$ simplifies this to

$$\frac{\partial [f]}{\partial t} = \frac{D_f + D_b (\alpha + \alpha^2 + \dots + \alpha^N)}{1 + \alpha + \alpha^2 + \dots + \alpha^N} \nabla^2 [f] = D_{eff} \nabla^2 [f]$$

where we have defined D_{eff} as

$$D_{eff} = \frac{D_f + D_b (\alpha + \alpha^2 + \dots + \alpha^N)}{1 + \alpha + \alpha^2 + \dots + \alpha^N} \quad (\text{Eq. S33})$$

Setting $D_b = 0$ (assume no mobility in the bound state) finally gives

$$\frac{D_f}{D_{eff}} = 1 + \alpha + \alpha^2 + \dots + \alpha^N = 1 + \sum_{i=1}^N \left(\frac{k_{on}^*}{k_{off}} \right)^i$$

(Eq. S34)

which is equation (5) reported in the main text. Note that (33) can be used to estimate the bound state mobility D_b if one relaxes the assumption that $D_b = 0$. In the above analysis, we have assumed symmetric sequential binding such that $K_1 = K_2 = \dots = K_N = k_{on}^* / k_{off}$. This assumption is easily relaxed by redefining α as α_i where

$$\alpha_i = \left(\frac{k_{on}^*}{k_{off}} \right)_1 \left(\frac{k_{on}^*}{k_{off}} \right)_2 \dots \left(\frac{k_{on}^*}{k_{off}} \right)_N = K_1 K_2 \dots K_N = \prod_{j=1}^i K_j \quad (\text{Eq. S35})$$

for $i = 1 \dots N$

The state fractions become $[d_i] \approx \alpha_i [f]$, which when supplied into the mass balance gives

$$[1 + \alpha_1 + \alpha_2 + \dots + \alpha_N] \frac{\partial [f]}{\partial t} = \{D_f + D_b [\alpha_1 + \alpha_2 + \dots + \alpha_N]\} \nabla^2 [f]$$

We can now define a new D_{eff} as

$$D_{eff} = \frac{D_f + D_b (\alpha_1 + \alpha_2 + \dots + \alpha_N)}{1 + \alpha_1 + \alpha_2 + \dots + \alpha_N} \quad (\text{Eq. S36})$$

which returns us to simple Fickian diffusion governed by the new D_{eff} , and the ratio D_f/D_{eff} is (neglecting bound mobility by setting $D_b = 0$)

$$\frac{D_f}{D_{eff}} = 1 + \alpha_1 + \alpha_2 + \dots + \alpha_N = 1 + \sum_{i=1}^N \left[\prod_{j=1}^i K_j \right] = 1 + K_1 + K_1 K_2 + \dots + K_1 K_2 \dots K_N$$

(Eq. S37)

Eq. S37 allows each equilibrium constant to be treated as an adjustable fitting parameter, and is used above to detect binding asymmetry ($K_1 > K_2$) by setting $D_{eff} = D_{obs}$ for PEcP, after fixing K_1 with the measurement from the PEc probe.

1.7.7 Fraction of elastically effective chains estimated from Phantom Network Theory

At 10% (w/v) the number density of chains is

$$\bar{n} = \rho \left(\frac{N_A}{M} \right) = 1.88 \times 10^{24} \text{ chains / m}^3$$

and the number density of bundles, assuming every endblock ends up in a pentamer, is

$$\bar{n}_b = \frac{2}{5} \bar{n} = 7.52 \times 10^{23} \text{ bundles / m}^3$$

From Phantom Network Theory, the fraction of elastically effective chains at 10% is given by ($f = 5$ for pentameric chain junctions):

$$\frac{G'_{\infty}}{G_{phantom}} = \bar{n} k T \left(1 - \frac{2}{f} \right) = 0.69$$

This set of equations can be used to estimate G' for gels prepared at different protein concentrations, as is shown in **Supplementary Figure 1.7**.

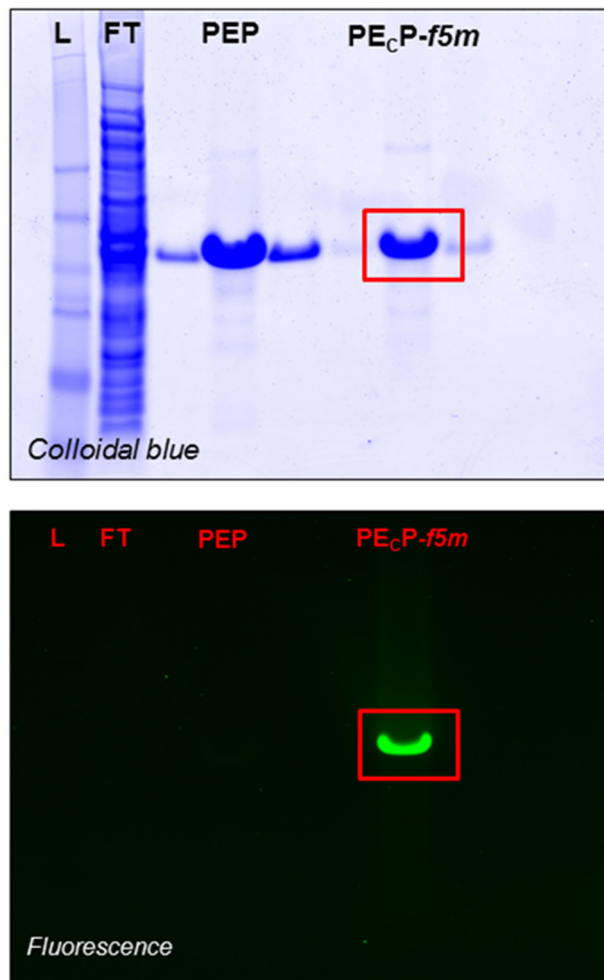
1.7.8 Supplementary Tables

Supplementary Table 1.1. Plasmids and sequence information for FRAP probes. Each “P” domain is highlighted in blue, and key mutations (Leu→Ala) or insertions (Cys) are highlighted in red and underlined. All protein coding sequences were confirmed by DNA sequencing.

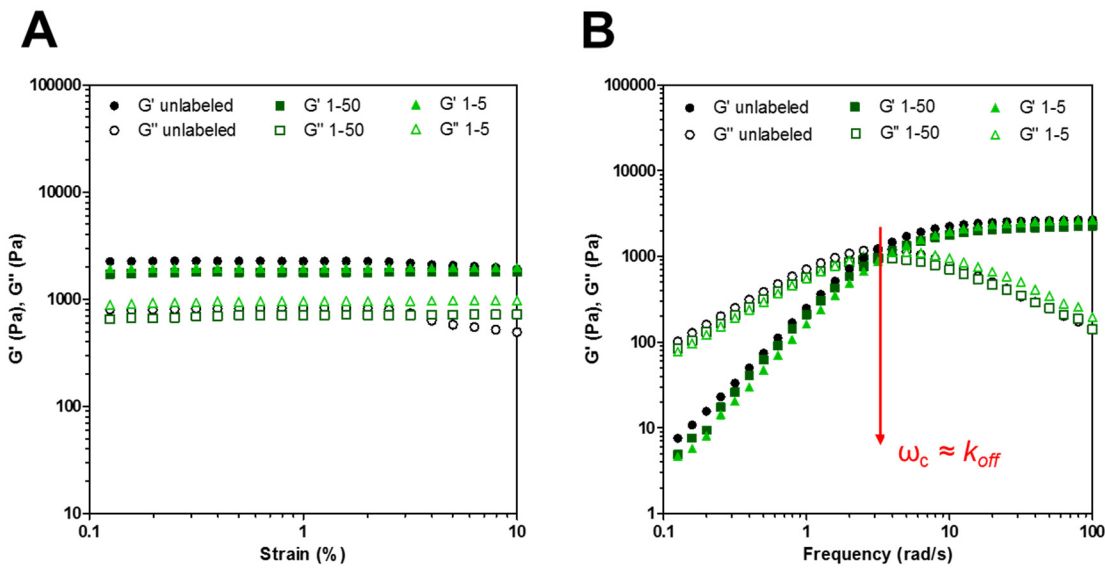
Supplementary Table 1.2. Quantification of Hil substitution level from MALDI-MS. Based on the above MALDI spectra, the degree of Hil substitution was calculated for different expression conditions (lanes 5-7 in **Supplementary Figure 1.8B**). In cultures containing Hil and depleted of Leu, a substitution level of $91.8 \pm 4.5\%$ was obtained. In cultures containing $500 \mu\text{M}$ Hil and $100 \mu\text{M}$ Leu, the substitution level was $53.2 \pm 10.6\%$. Cultures grown without Hil contained only Leu. The incorporation levels were determined by integration of MALDI peaks for three peptide fragments.

Peptide	<i>Expected MW (Da)</i>		% of Hil-substituted residues		
			μM	Leu	Leu + Hil
	[Leu]	300	100	0	
	+ Leu	+ Hil	[Hil]	0	500
ELLR	529.6	557.7		-	65.5%
EITFLK	749.9	763.9		-	46.9%
ELQETNAALQDVR	1486.6	1514.6		-	47.1%
			avg	53.2%	91.8%
			<i>std</i>	10.6%	4.5%

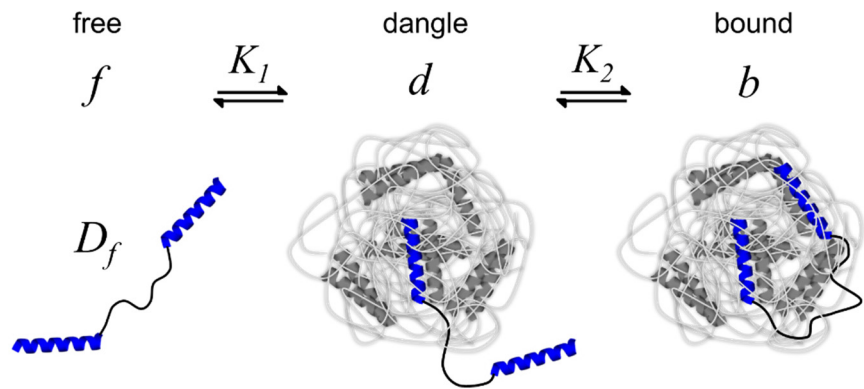
1.7.9 Supplementary Figures



Supplementary Figure 1.1. Site-specific labeling of PE_cP. SDS-PAGE analysis of unpurified and purified PEP and PE_cP constructs. (Top) Colloidal blue staining reveals the following bands: **L**, ladder; **FT**, flow-through from His-purification; **PEP**, elution of purified protein from Ni-NTA column; **PE_cP**, analogous elution of purified PE_cP-f5m (labeled with fluorescein-5-maleimide). (Bottom) Fluorescence analysis of the same gel shows that fluorophore is conjugated to PE_cP-f5m.

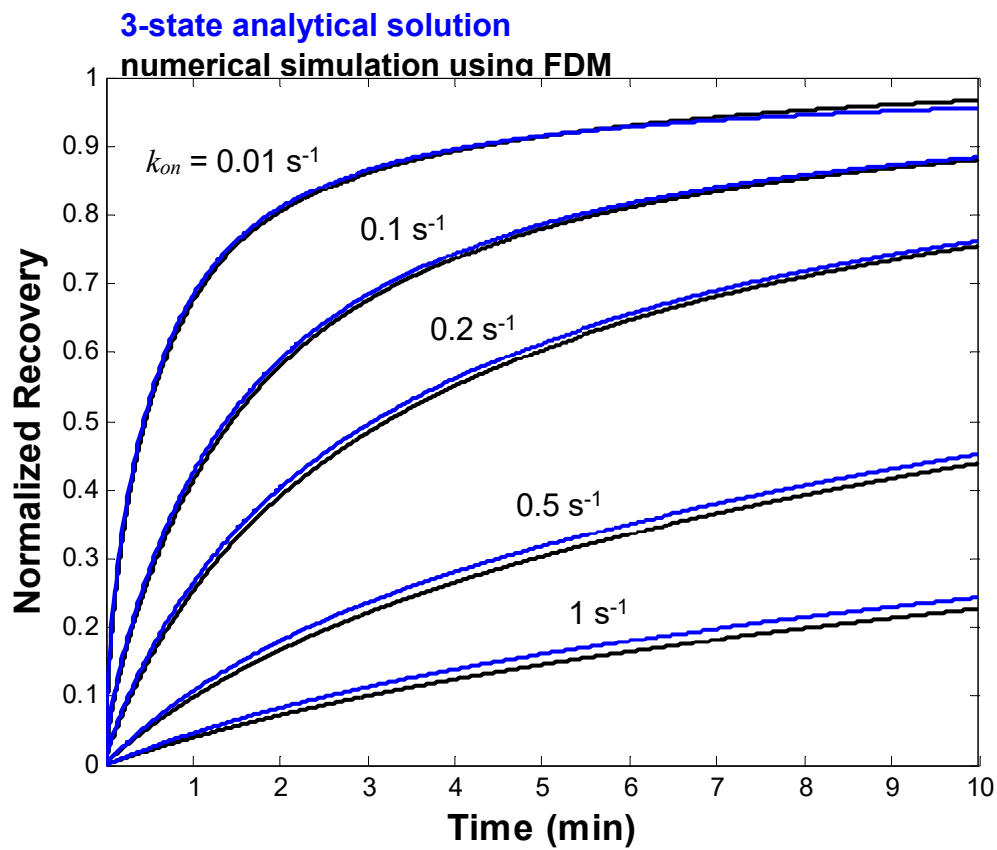


Supplementary Figure 1.2. Low probe concentrations do not affect network rheology. Labeling with PECP-*f5m* (1:5 or 1:50) minimally affects the rheological behavior of 10% PEP networks. **(A)** Strain sweeps at 10 rad s^{-1} show minimal variation in the elastic (G') and loss (G'') moduli in a linear regime between 0.1 and 10% strain. **(B)** Frequency sweeps at 1% strain show similar frequency-dependent behavior for labeled and unlabeled gels. Data were collected on a parallel plate rheometer (15 mm plate diameter) and a gap width of $250 \mu\text{m}$. The crossover frequency ω_c , which also remains unchanged upon labeling, can be taken as an approximation of the off rate k_{off} (see discussion above).

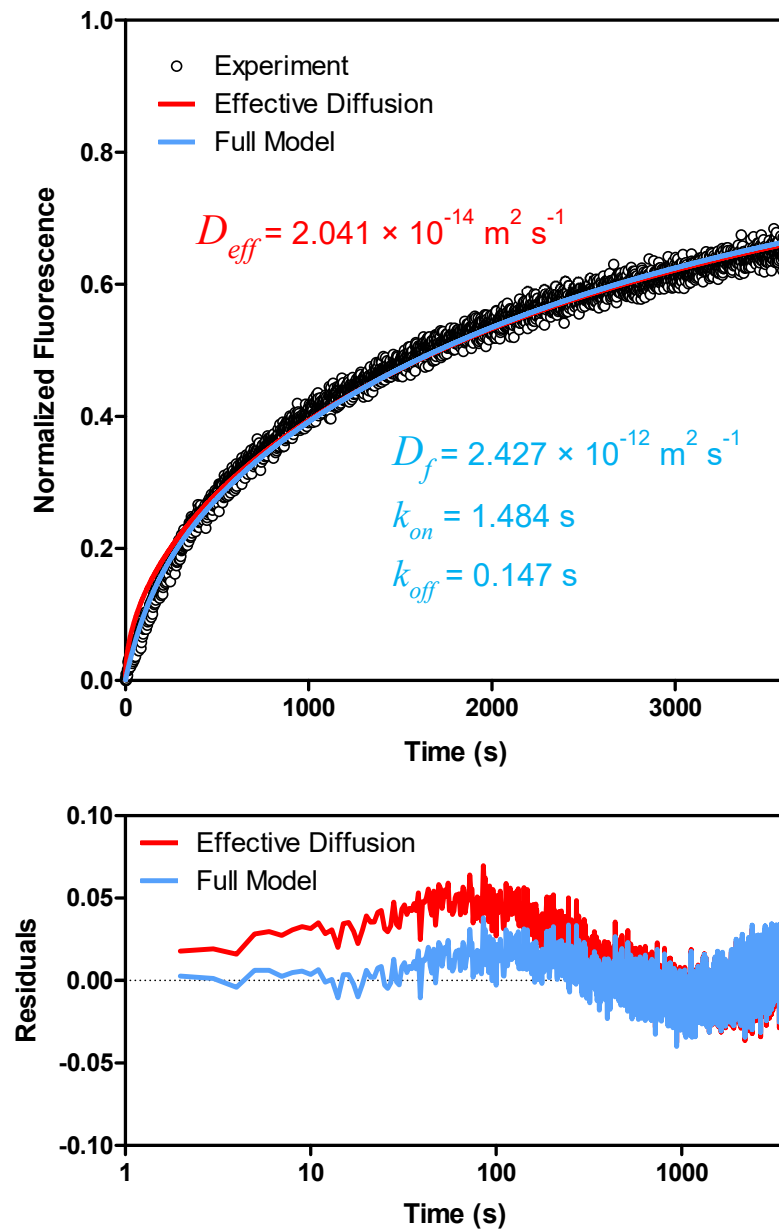


Supplementary Figure 1.3. Graphical representation of the 3-state reaction-diffusion model.

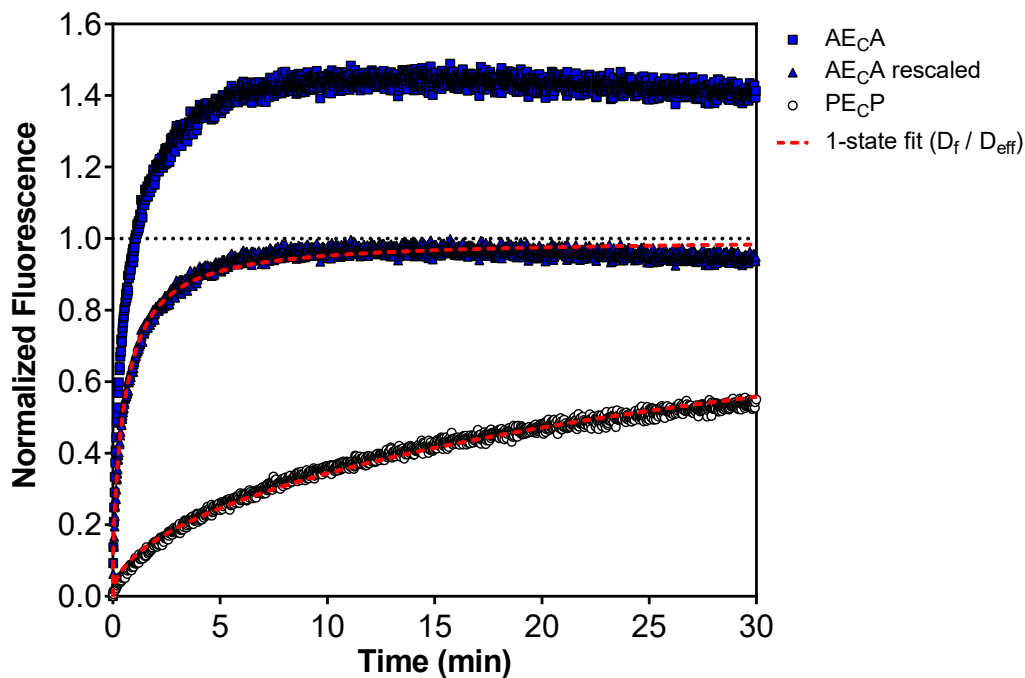
Free polymer chains f diffuse with diffusion coefficient D_f within the network. A chain with one arm bound enters the dangle state d . Upon binding of both arms, the chain is in the bound state b and, like the dangling chains, assumed to have no spatial mobility because interchain crosslinks constrain its motion. Interconversion between these three states is governed by the equilibrium constants K_1 and K_2 . In developing the analytical solution below, we assume that $K_1 \approx K_2 = k_{on}^*/k_{off}$. This assumption is considered in detail in **Section 1.4**, and can be relaxed (see **Eq. S33 – S37**).



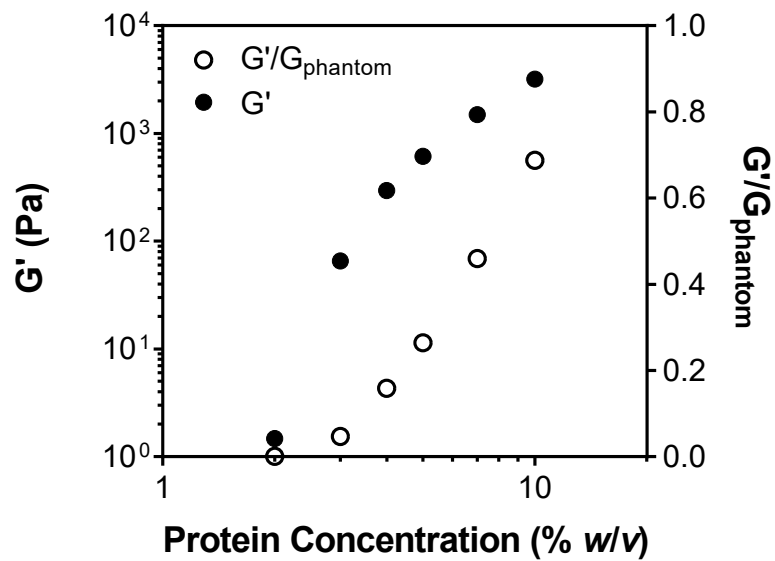
Supplementary Figure 1.4. Validation of the analytical solution to the 3-state model. Simulated fluorescence recovery curves obtained by using a finite difference method (FDM, black) and by numerical inversion of (Eq. S23), (blue). The parameters used to obtain the simulated curves were $a = 10\text{ }\mu\text{m}$, $D_f = 1\text{ }\mu\text{m}^2\text{ s}^{-1}$ and $k_{off} = 0.1\text{ s}^{-1}$. The values used for k_{on} are displayed above their corresponding curves. All simulations were performed in MATLAB. The code used to numerically invert the Laplace-domain solution was *invlap.m*, which is included below. The small divergence between curves at higher values of k_{on} (close to $\sim 1\text{ s}^{-1}$) is a result of the finite space discretization in the numerical FDM implementation. The divergence disappears when finer mesh sizes are chosen. Furthermore, simulations out to 60 min indicate that the divergence does not continue to grow at long times.



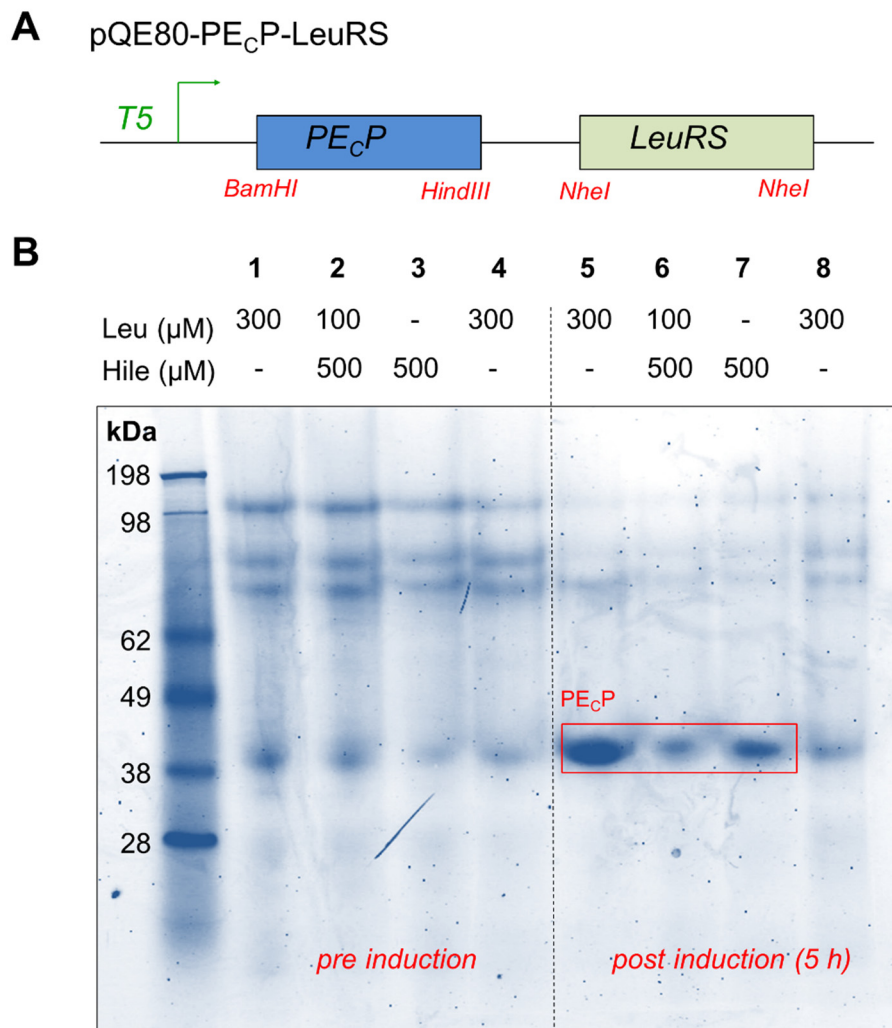
Supplementary Figure 1.5. Simulated FRAP curves fit to experimental data (shown for a 10% PEP gel labeled with PE_CP). The experimental recovery curve shows excellent agreement with both the full model simulation (blue) and the simplified, effective diffusion model (red). The key parameters extracted from these fits are also listed (*Top*). A residuals analysis of the two curves shows that the full model results in a slightly better fit in this case. In both cases, RMS of all the residuals is < 1 (*Bottom*).



Supplementary Figure 1.6. Fluorescence recovery curves for AE_CA and PE_CP in 10% PEP networks. The final fluorescence intensity for AE_CA bleach spots often exceeded the original intensity before the bleach. As a result, AE_CA (and E_C) recovery curves were typically rescaled before curve fitting such that the maximum fluorescence intensity was equal to 1. Curves for AE_CA and PE_CP were fit to the 1-state effective diffusion model (Equation S23 with $k_{on}^*/k_{off} \approx 0$, or Equations S25 and S30) in order to get D_f for and D_{eff} for PE_CP. This unusual recovery behavior is attributed to the LCST behavior of elastin-like polypeptides, and is characterized further in Chapter 3.

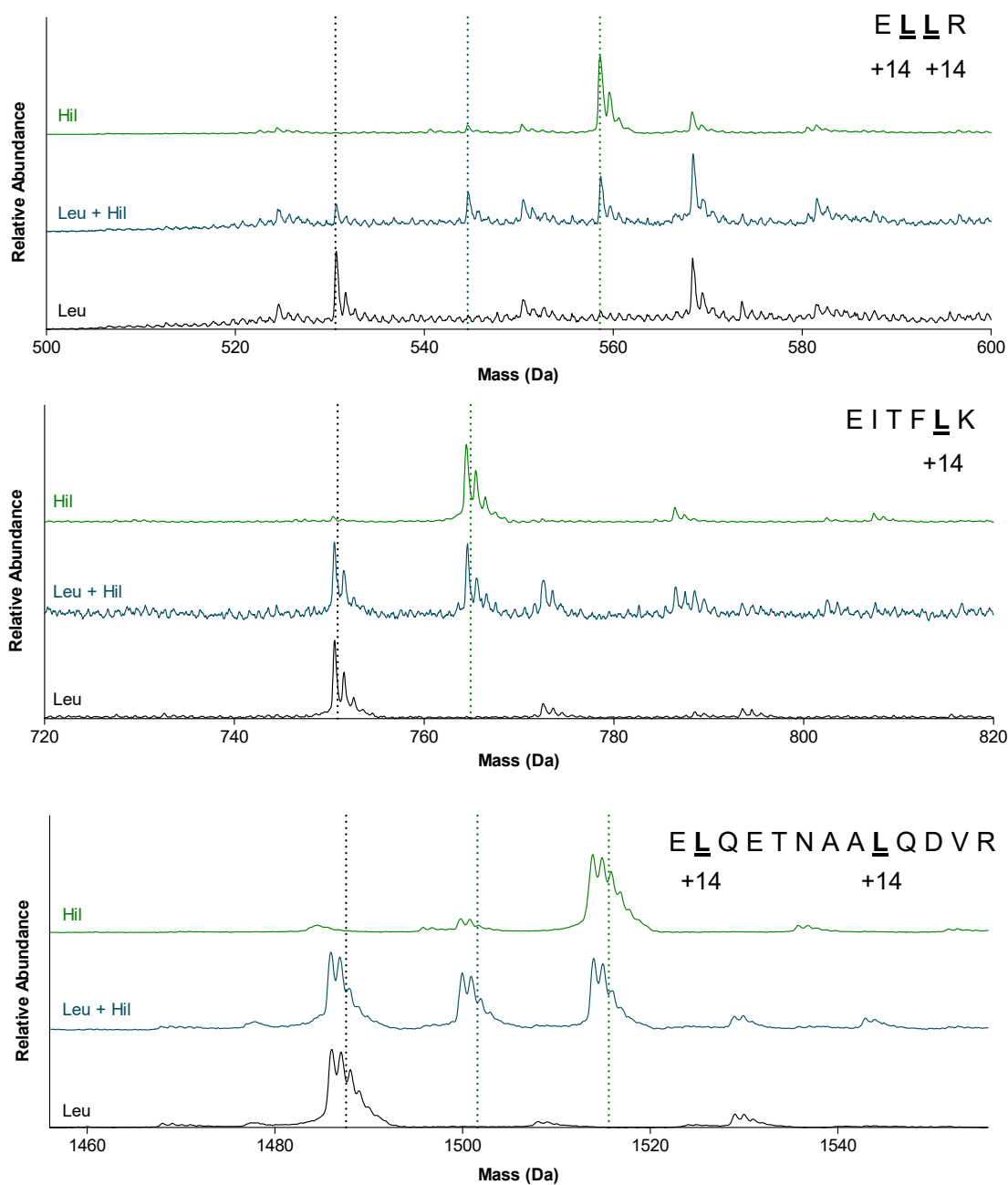


Supplementary Figure 1.7. Fraction of elastically effective chains estimated from phantom network theory ($G'/G_{phantom} = 0.69$ at 10%). Chains in the bound state include both bridges (B) and loops (L), such that $[b]_{eq} = [B] + [L]$. The simulation described above gives $[B] = 0.70$, similar to the experimental $G'/G_{phantom}$.

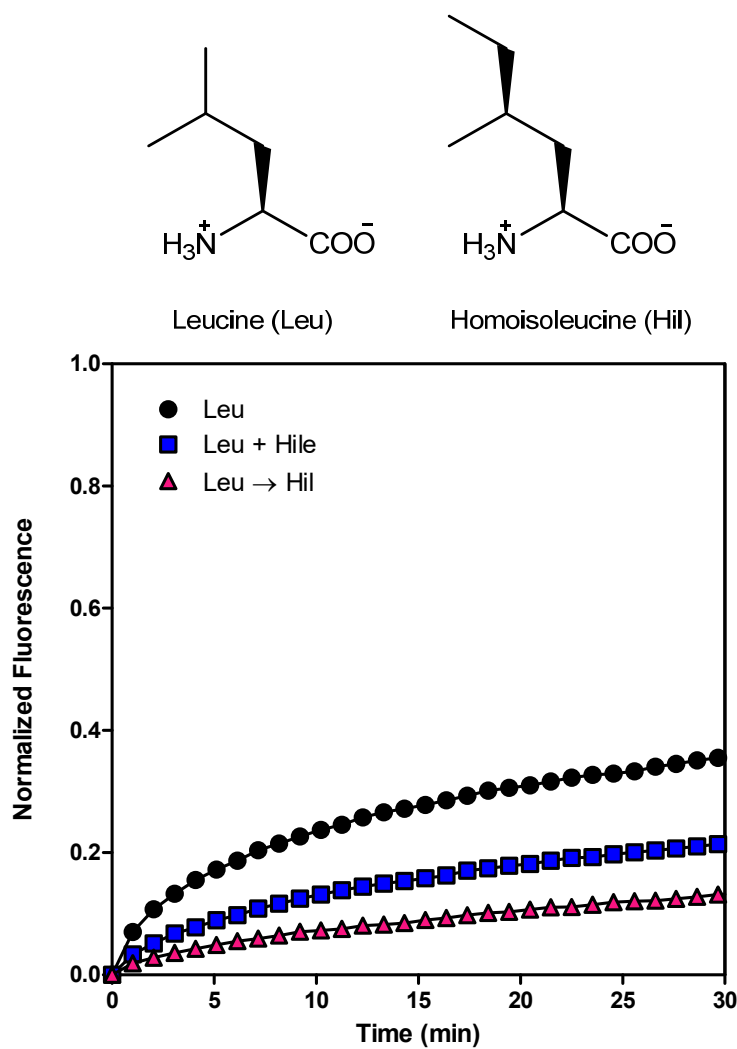


Supplementary Figure 1.8. Validation of expression cassette for incorporation of Hil into PE_CP.

(A) To prepare the plasmid pQE80-LeuRS-PEcP, the PEcP gene was PCR amplified and ligated into pQE-80L-LeuRS between *BamHI* and *HindIII* restriction sites. The gene coding for LeuRS is downstream of PEcP flanked by *NheI* restriction sites. Its expression is constitutively controlled by its endogenous *E. coli* promoter, whereas PEcP is under T5 control and is inducible with IPTG. (B) 1 L expression cultures of strains carrying pQE80-PEcP-LeuRS in M9 minimal media supplemented with Hil: **1-4**, pre-induction cultures grown in 19AA + Leu; **5-7**, cultures were shifted into M9 media containing 19AA and the indicated amounts of Leu and Hil. Protein expression was induced with 1 mM IPTG and the cultures collected after 5 h; **8**, non-induced control. Strong PEcP expression can be seen after 5 h.



Supplementary Figure 1.9. MALDI-MS of tryptic peptides containing Hil. PE_CP was purified from Hil expression lysates and subject to trypsin digestion followed by MALDI-MS. The spectra corresponding to three quantified peptides are presented above. A Hil substitution may be identified by a *m/z* shift of 14 Da arising from the presence of an additional methylene group. The peptides and their expected masses with and without Hil are listed in **Supplementary Table 1.2**. Spectral analysis indicates a maximum Leu → Hil replacement level of **91.8 ± 4.5%**.



Supplementary Figure 1.10. Tuning the fluorescence recovery rate with Hil by controlling the level of incorporation of Hil. Fluorescence recovery curves of a 10% PEP gel labeled with fluorescent PE_CP-Hil probes at a mass ratio of 1:5 PE_CP to PEP (i.e. 20% of the network consists of fluorescent probe). The blue curve (Leu + Hil) shows the recovery curve for 53% Hil substitution, and the magenta curve (Leu → Hil) shows the recovery curve for 92% substitution (see **Supplementary Table 1.2** for exact incorporation levels). The degree of substitution provides a means of tuning the fluorescence recovery rate.

1.8 References

1. S. Banta, I. R. Wheeldon, M. Blenner, Protein Engineering in the Development of Functional Hydrogels. *Annu Rev Biomed Eng* **12**, 167-186 (2010).
2. W. A. Petka, J. L. Harden, K. P. McGrath, D. Wirtz, D. A. Tirrell, Reversible hydrogels from self-assembling artificial proteins. *Science* **281**, 389-392 (1998).
3. S. Creutz, J. van Stam, F. C. De Schryver, R. Jerome, Dynamics of poly((dimethylamino)alkyl methacrylate-block-sodium methacrylate) micelles. Influence of hydrophobicity and molecular architecture on the exchange rate of copolymer molecules. *Macromolecules* **31**, 681-689 (1998).
4. Z. L. Li, E. E. Dormidontova, Equilibrium chain exchange kinetics in block copolymer micelle solutions by dissipative particle dynamics simulations. *Soft Matter* **7**, 4179-4188 (2011).
5. T. Annable, R. Buscall, R. Ettelaie, D. Whittlestone, The Rheology of Solutions of Associating Polymers - Comparison of Experimental Behavior with Transient Network Theory. *J Rheol* **37**, 695-726 (1993).
6. T. van der Heijden *et al.*, Homologous recombination in real time: DNA strand exchange by RecA. *Mol Cell* **30**, 530-538 (2008).
7. J. T. Holthausen, C. Wyman, R. Kanaar, Regulation of DNA strand exchange in homologous recombination. *DNA Repair* **9**, 1264-1272 (2010).
8. W. Shen, K. C. Zhang, J. A. Kornfield, D. A. Tirrell, Tuning the erosion rate of artificial protein hydrogels through control of network topology. *Nat. Mater.* **5**, 153-158 (2006).
9. W. Shen, J. A. Kornfield, D. A. Tirrell, Dynamic properties of artificial protein hydrogels assembled through aggregation of leucine zipper peptide domains. *Macromolecules* **40**, 689-692 (2007).
10. E. K. O'Shea, R. Rutkowski, W. F. Stafford, P. S. Kim, Preferential Heterodimer Formation by Isolated Leucine Zippers from Fos and Jun. *Science* **245**, 646-648 (1989).
11. E. K. O'Shea, R. Rutkowski, P. S. Kim, Evidence That the Leucine Zipper Is a Coiled Coil. *Science* **243**, 538-542 (1989).
12. W. H. Landschulz, P. F. Johnson, S. L. McKnight, The Leucine Zipper - a Hypothetical Structure Common to a New Class of DNA-Binding Proteins. *Science* **240**, 1759-1764 (1988).

13. B. D. Olsen, J. A. Kornfield, D. A. Tirrell, Yielding Behavior in Injectable Hydrogels from Telechelic Proteins. *Macromolecules* **43**, 9094-9099 (2010).
14. S. J. Ryan, A. J. Kennan, Variable stability heterodimeric coiled-coils from manipulation of electrostatic interface residue chain length. *J. Am. Chem. Soc.* **129**, 10255-10260 (2007).
15. J. D. Steinkruger, D. N. Woolfson, S. H. Gellman, Side-Chain Pairing Preferences in the Parallel Coiled-Coil Dimer Motif: Insight on Ion Pairing between Core and Flanking Sites. *J. Am. Chem. Soc.* **132**, 7586-7588 (2010).
16. H. Wendt, C. Berger, A. Baici, R. M. Thomas, H. R. Bosshard, Kinetics of Folding of Leucine-Zipper Domains. *Biochemistry* **34**, 4097-4107 (1995).
17. D. L. Daugherty, S. H. Gellman, A fluorescence assay for leucine zipper dimerization: Avoiding unintended consequences of fluorophore attachment. *J. Am. Chem. Soc.* **121**, 4325-4333 (1999).
18. B. L. Sprague, R. L. Pego, D. A. Stavreva, J. G. McNally, Analysis of binding reactions by fluorescence recovery after photobleaching. *Biophys J* **86**, 3473-3495 (2004).
19. B. M. Mayr, E. Guzman, M. Montminy, Glutamine rich and basic region/leucine zipper (bZIP) domains stabilize cAMP-response element-binding protein (CREB) binding to chromatin. *J Biol Chem* **280**, 15103-15110 (2005).
20. J. G. McNally, Quantitative FRAP in analysis of molecular binding dynamics in vivo. *Method Cell Biol* **85**, 329-351 (2008).
21. Y. A. Li *et al.*, Mobility of lysozyme inside oxidized starch polymer microgels. *Soft Matter* **7**, 1926-1935 (2011).
22. S. C. DeSmedt *et al.*, Diffusion of macromolecules in dextran methacrylate solutions and gels as studied by confocal scanning laser microscopy. *Macromolecules* **30**, 4863-4870 (1997).
23. M. C. Branco, D. J. Pochan, N. J. Wagner, J. P. Schneider, Macromolecular diffusion and release from self-assembled beta-hairpin peptide hydrogels. *Biomaterials* **30**, 1339-1347 (2009).
24. F. Herbst, S. Seiffert, W. H. Binder, Dynamic supramolecular poly(isobutylene)s for self-healing materials. *Polym Chem* **3**, 3084-3092 (2012).

25. P. Gribbon, T. E. Hardingham, Macromolecular diffusion of biological polymers measured by confocal fluorescence recovery after photobleaching. *Biophys J* **75**, 1032-1039 (1998).
26. P. Gribbon, B. C. Heng, T. E. Hardingham, The molecular basis of the solution properties of hyaluronan investigated by confocal fluorescence recovery after photobleaching. *Biophys J* **77**, 2210-2216 (1999).
27. V. N. Malashkevich, R. A. Kammerer, V. P. Efimov, T. Schulthess, J. Engel, The crystal structure of a five-stranded coiled coil in COMP: A prototype ion channel? *Science* **274**, 761-765 (1996).
28. P. A. Perry, M. A. Fitzgerald, R. G. Gilbert, Fluorescence recovery after photobleaching as a probe of diffusion in starch systems. *Biomacromolecules* **7**, 521-530 (2006).
29. S. Tang, M. J. Glassman, S. Li, S. Socrate, B. D. Olsen, Oxidatively Responsive Chain Extension to Entangle Engineered Protein Hydrogels. *Macromolecules* **47**, 791-799 (2014).
30. D. M. Sompasis, Theoretical-Analysis of Fluorescence Photobleaching Recovery Experiments. *Biophys J* **41**, 95-97 (1983).
31. K. J. Hollenbeck, 1998. INVLAP.M: A MATLAB function for numerical inversion of Laplace transforms by the de Hoog algorithm.
http://www.mathworks.com/matlabcentral/answers/uploaded_files/1034/invlap.m.
32. W. B. Zhang, F. Sun, D. A. Tirrell, F. H. Arnold, Controlling Macromolecular Topology with Genetically Encoded SpyTag-SpyCatcher Chemistry. *J. Am. Chem. Soc.* **135**, 13988-13997 (2013).
33. B. Zakeri *et al.*, Peptide tag forming a rapid covalent bond to a protein, through engineering a bacterial adhesin. *Proc Natl Acad Sci USA* **109**, E690-E697 (2012).
34. G. M. Cruise, D. S. Scharp, J. A. Hubbell, Characterization of permeability and network structure of interfacially photopolymerized poly(ethylene glycol) diacrylate hydrogels. *Biomaterials* **19**, 1287-1294 (1998).
35. L. M. Weber, C. G. Lopez, K. S. Anseth, Effects of PEG hydrogel crosslinking density on protein diffusion and encapsulated islet survival and function. *J Biomed Mater Res A* **90**, 720-729 (2009).
36. K. Engberg, C. W. Frank, Protein diffusion in photopolymerized poly(ethylene glycol) hydrogel networks. *Biomed Mater* **6**, 055006 (2011).

37. J. A. Zitzewitz, O. Bilsel, J. B. Luo, B. E. Jones, C. R. Matthews, Probing the Folding Mechanism of a Leucine-Zipper Peptide by Stopped-Flow Circular-Dichroism Spectroscopy. *Biochemistry* **34**, 12812-12819 (1995).
38. L. R. Patel, T. Curran, T. K. Kerppola, Energy-Transfer Analysis of Fos-Jun Dimerization and DNA-Binding. *Proc Natl Acad Sci USA* **91**, 7360-7364 (1994).
39. S. Ozeki, T. Kato, M. E. Holtzer, A. Holtzer, The Kinetics of Chain Exchange in 2-Chain Coiled Coils - Alpha-Alpha-Tropomyosin and Beta-Beta-Tropomyosin. *Biopolymers* **31**, 957-966 (1991).
40. S. Dalal, D. Canet, S. E. Kaiser, C. M. Dobson, L. Regan, Conservation of mechanism, variation of rate: folding kinetics of three homologous four-helix bundle proteins. *Protein Eng Des Sel* **21**, 197-206 (2008).
41. S. Y. Park, C. M. Quezada, A. M. Bilwes, B. R. Crane, Subunit exchange by CheA histidine kinases from the mesophile *Escherichia coli* and the thermophile *Thermotoga maritima*. *Biochemistry* **43**, 2228-2240 (2004).
42. H. Wendt, A. Baici, H. R. Bosshard, Mechanism of Assembly of a Leucine-Zipper Domain. *J. Am. Chem. Soc.* **116**, 6973-6974 (1994).
43. S. K. Gunasekar *et al.*, N-Terminal Aliphatic Residues Dictate the Structure, Stability, Assembly, and Small Molecule Binding of the Coiled-Coil Region of Cartilage Oligomeric Matrix Protein. *Biochemistry* **48**, 8559-8567 (2009).
44. K. Beck, J. E. Gambee, C. A. Bohan, H. P. Bachinger, The C-terminal domain of cartilage matrix protein assembles into a triple-stranded alpha-helical coiled-coil structure. *J Mol Biol* **256**, 909-923 (1996).
45. K. Kremer, G. S. Grest, Dynamics of entangled linear polymer melts: A molecular-dynamics simulation. *J Chem Phys* **92**, 5057-5086 (1990).
46. W. Shen, J. A. Kornfield, D. A. Tirrell, Structure and mechanical properties of artificial protein hydrogels assembled through aggregation of leucine zipper peptide domains. *Soft Matter* **3**, 99-107 (2007).
47. S. C. Tang, M. Z. Wang, B. D. Olsen, Anomalous Self-Diffusion and Sticky Rouse Dynamics in Associative Protein Hydrogels. *J. Am. Chem. Soc.* **137**, 3946-3957 (2015).
48. P. B. Harbury, T. Zhang, P. S. Kim, T. Alber, A Switch between 2-Stranded, 3-Stranded and 4-Stranded Coiled Coils in Gcn4 Leucine-Zipper Mutants. *Science* **262**, 1401-1407 (1993).

49. J. A. Van Deventer, J. D. Fisk, D. A. Tirrell, Homoisoleucine: A Translationally Active Leucine Surrogate of Expanded Hydrophobic Surface Area. *ChemBioChem* **12**, 700-702 (2011).
50. L. J. Dooling, M. E. Buck, W. B. Zhang, D. A. Tirrell, Programming Molecular Association and Viscoelastic Behavior in Protein Networks. *Adv Mater* **28**, 4651-4657 (2016).
51. J. Braga, J. G. McNally, M. Carmo-Fonseca, A reaction-diffusion model to study RNA motion by quantitative fluorescence recovery after photobleaching. *Biophys J* **92**, 2694-2703 (2007).